

1 **The Changing Eigenfrequency Continuum during Geomagnetic**
2 **Storms: Implications for Plasma Mass Dynamics and ULF Wave**
3 **Coupling**

4 **S. J. Wharton¹, I. J. Rae², J. K. Sandhu², M.-T. Walach³, D. M. Wright¹, and T. K. Yeoman¹**

5 ¹Department of Physics and Astronomy, University of Leicester, Leicester, UK

6 ²Mullard Space Science Laboratory, University College London, Dorking, UK

7 ³Lancaster University, Bailrigg, Lancaster, UK

8 **Key Points:**

- 9 • We measure the average storm-time evolution of field line eigenfrequencies, ac-
10 counting for diurnal variation
- 11 • Lower eigenfrequencies during the main phase for $L > 4$ are due to a weaker mag-
12 netic field and enhanced plasma mass density
- 13 • Higher eigenfrequencies during the main phase for $L < 4$ are due to plasmaspheric
14 erosion

Abstract

Geomagnetic storms are one of the most energetic space weather phenomena. Previous studies have shown that the eigenfrequencies of closed magnetic field lines in the inner magnetosphere decrease during storm times. This change suggests either a reduction in the magnetic field strength and/or an increase in its plasma mass density distribution. We investigate the changes in local eigenfrequencies by applying a superposed multiple-epoch analysis to cross-phase spectra from 132 geomagnetic storms. Six ground magnetometer pairs are used to investigate variations from approximately $3 < L < 7$ and across the whole dayside sector. We find that at $L > 4$, the eigenfrequencies decrease by as much as 50% relative to their quiet time values. Both a decrease in magnetic field strength and an increase in plasma mass density, in some locations by more than a factor of two, are responsible for this reduction. The enhancement of the ring current and an increase in Oxygen ion density could explain these observations. At $L < 4$, the eigenfrequencies increase due to the decrease in plasma mass density caused by plasmaspheric erosion.

Plain Language Summary

Periods of intense solar wind can cause geomagnetic storms, large disturbances of the magnetosphere. Previous studies have shown that this can decrease the resonant frequencies of magnetic field lines with the Earth's magnetosphere. We perform a large statistical study on 132 storms to investigate this in order to understand the physics that drives this change. We find that the resonant frequencies typically decrease on field lines where $L > 4$ due to a weaker magnetic field caused by an enhanced ring current and a higher plasma mass density. We suggest the higher plasma mass density could be caused by an increase in Oxygen ions. At $L < 4$, the eigenfrequencies increase due to a drop in plasma mass density caused by plasmaspheric erosion.

1 Introduction

Geomagnetic storms are prolonged periods of intense solar wind - magnetosphere coupling that compress the Earth's magnetosphere, energize the magnetosphere - ionosphere system, and result in strong enhancements of the ring current, amongst other phenomena. These have been documented since the 19th century [Stewart, 1861]. Coronal mass ejections and corotating interaction regions are the most common drivers of geo-

45 magnetic storms. The most intense coupling happens if the interplanetary magnetic field
 46 (IMF) is orientated southwards and results in enhanced plasma convection within the mag-
 47 netosphere [Akasofu *et al.*, 1963; Gonzalez *et al.*, 1994]. During these disturbances, large
 48 quantities of energy are released from the Earth's magnetotail, often causing increased
 49 substorm activity [e.g., Hutchinson *et al.*, 2011] and enhancing the Earth's radiation belts
 50 [e.g., Murphy *et al.*, 2016].

51 The presence of a geomagnetic storm is usually monitored using ring current in-
 52 dices, most commonly the Dst [http://wdc.kugi.kyoto-u.ac.jp/dst/dir/dst2/
 53 onDstindex.html](http://wdc.kugi.kyoto-u.ac.jp/dst/dir/dst2/onDstindex.html) or the Sym-H [Iyemori, 1990] index. Ring current indices are de-
 54 termined from the perturbation of the horizontal magnetic field strength using a set of
 55 ground-based magnetometers located at mid latitudes. These locations map to inside the
 56 ring current region of space where they largely avoid other current systems. A storm usu-
 57 ally has three observable phases in the ring current indices (see Figure 1). During the ini-
 58 tial phase, the ring current index increases due to the enhancements in the magnetopause
 59 currents as the magnetosphere is compressed, which increases the magnetic field strength
 60 on the ground. During the main phase of the storm, the ring current intensifies, which re-
 61 sults in a sharp drop in the ring current index due to the weakened magnetic field. The
 62 recovery phase usually lasts several days as the ring current decays. Hence, a sharp de-
 63 crease in the Sym-H index is indicative of a geomagnetic storm [e.g., Chapman and Fer-
 64 raro, 1930; Akasofu *et al.*, 1963].

65 Magnetic flux tubes, or field lines, can support standing Alfvén waves. The eigenfre-
 66 quencies on any given flux tube depend upon the flux tube length, wave polarisation and
 67 the Alfvén speed v_A , which in turn depends on the magnetic field strength, B , and plasma
 68 mass density, ρ , of the flux tube [Cummings *et al.*, 1969]. The dependencies on v_A are
 69 given by

$$v_A = \frac{B}{\sqrt{\mu_0 \rho}} \quad (1)$$

70 where μ_0 is the permeability of free space. The eigenfrequencies of any given flux
 71 tube thus depend upon the relationship between these three parameters: eigenfrequencies
 72 will increase if the magnetic field strength increases, the plasma mass density decreases,
 73 or the flux tube decreases in length.

74 **1.1 Eigenfrequencies during Storm Times**

75 Several studies have observed that the eigenfrequencies of closed magnetic field
76 lines decrease as the ring current index decreases (becomes more negative). *Wild et al.*
77 [2005] predicted this by using the time of flight technique to calculate eigenfrequencies in
78 a T96 magnetic field model [*Tsyganenko*, 1996] parameterised by the Dst index. *Sandhu*
79 *et al.* [2018a] used the same technique but with the more realistic plasma mass density
80 model of *Sandhu et al.* [2017] based on 12 years of Cluster data ($L > 5.9$) that could be
81 parameterised by the Dst index and found the same result. Most recently, *Wharton et al.*
82 [2019a] performed a statistical analysis of eigenfrequencies measured by the cross-phase
83 technique applied to ground magnetometers and found that the eigenfrequencies decreased
84 when the Sym-H index was reduced for $L > 4$.

85 Other studies have investigated single geomagnetic storm events. *Kale et al.* [2009];
86 *Takasaki et al.* [2006] and *Chi et al.* [2005] all looked at the Halloween storm event in Oc-
87 tober 2003 and each found that the eigenfrequency decreased after a sudden storm com-
88 mencement. *Du et al.* [2005] also found an eigenfrequency decrease for a storm in July
89 2000, *Lee et al.* [2007] for the March 1991 storm and *Rae et al.* [2019] for the March 2013
90 storm. *Warner and Orr* [1979]; *Engebretson and Cahill Jr.* [1981] and *Takahashi et al.*
91 [2002] are amongst others to have observed eigenfrequencies decrease with increasing ge-
92 omagnetic activity at the latitudes investigated in this study.

93 **1.2 Corresponding Changes in Plasma Mass Density**

94 The plasma mass density model of *Sandhu et al.* [2017] revealed that during peri-
95 ods of low Dst index, the plasma mass density decreased, despite the average ion mass
96 increasing. This was because the electron number density decreased. A reduced plasma
97 mass density would increase the eigenfrequencies. However, *Sandhu et al.* [2018a] used
98 this model and the T96 magnetic field model to show that the eigenfrequencies decreased
99 for low Dst values. This was because the reduction in the magnetic field strength created
100 by an enhanced ring current was dominant in determining the eigenfrequencies over the
101 reduced plasma mass density. Several other studies have shown that the plasma mass den-
102 sity decreases during enhanced geomagnetic activity [e.g., *Dent et al.*, 2006; *Denton et al.*,
103 2006; *Menk et al.*, 2014; *Corpo et al.*, 2018].

104 However, it has also been shown that the plasma mass density increases in response
 105 to increased geomagnetic activity [*Takahashi et al.*, 2002, 2006, 2010], and *Min et al.*
 106 [2013] showed that the plasma mass density barely changes. *Chi et al.* [2005]; *Takasaki*
 107 *et al.* [2006], and *Kale et al.* [2009] also determined that the plasma mass density increased
 108 after the sudden storm commencement. Equation (1) shows that if the plasma mass den-
 109 sity increases, then changes in both the plasma mass density and magnetic field strength
 110 are acting in cooperation to decrease the eigenfrequencies by reducing the Alfvén speed.
 111 In this scenario, just considering the change in magnetic field strength would not fully ac-
 112 count for the decrease in eigenfrequency.

113 1.3 The Objectives of this Study

114 Studies based on correlating eigenfrequencies with a ring current index [e.g., *Sandhu*
 115 *et al.*, 2017; *Wharton et al.*, 2019a] do not fully capture the eigenfrequency evolution through-
 116 out a geomagnetic storm's three phases. Eigenfrequency data taken during the main and
 117 recovery phases will be combined when binning by only the value of a ring current index.
 118 For example, a bin containing all samples taken when the Dst index was -80 nT would
 119 include samples corresponding to both the main and recovery phases of a storm. It is im-
 120 portant to consider the phases separately as each storm phase is associated with different
 121 magnetospheric processes. The statistics will also be dominated by data in the recovery
 122 phase, as this is typically the longest phase. Hence, the results will not typically describe
 123 what is happening in the main phase of the storm.

124 Other studies have looked at how the eigenfrequencies vary for specific storms [e.g.,
 125 *Lee et al.*, 2007; *Rae et al.*, 2019] to explore the time evolution. However, these studies
 126 do not provide information on whether the storms are representative of the statistically
 127 average storm, especially as these studies focussed on more extreme events. Any storm
 128 related trends in the data will also be contaminated by diurnal effects. For example, if
 129 observations beginning in the morning observe an eigenfrequency decrease throughout
 130 the day as a storm is progressing, it is difficult to determine how much of this decrease
 131 is due to the storm and how much is due to the expected diurnal variation for a single
 132 event. The eigenfrequencies normally decrease when moving into the afternoon sector
 133 [e.g., *Chappell et al.*, 1971; *Chi et al.*, 2013; *Sandhu et al.*, 2018b; *Wharton et al.*, 2019a].
 134 Data from multiple storms are required to disentangle these two factors influencing the
 135 change in eigenfrequency.

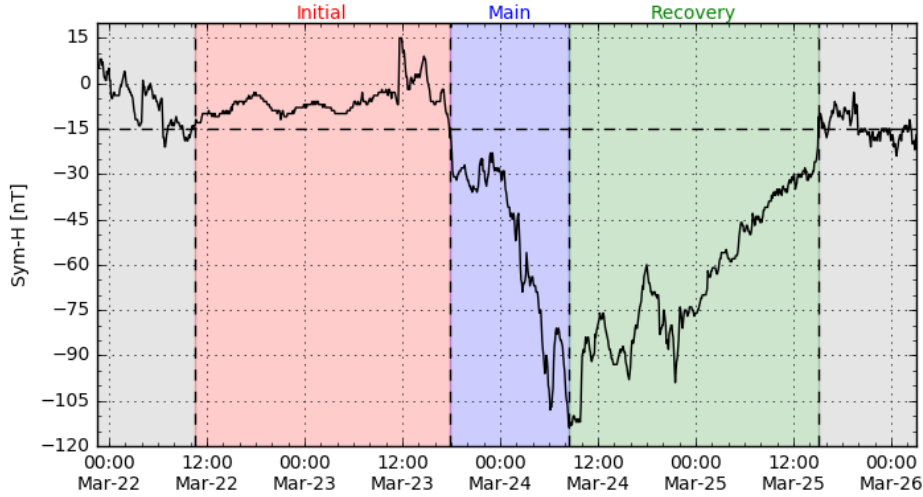
136 A statistical study of a large number of storms enables us to determine the average
 137 trends in eigenfrequencies during storms and to reduce the diurnal variation. 132 storms
 138 are identified using the algorithm of *Walach and Grocott* [2019]. The cross-phase tech-
 139 nique of *Wharton et al.* [2018, 2019b] is used to measure the eigenfrequencies and the
 140 superposed multiple-epoch analysis method employed by *Hutchinson et al.* [2011] is used
 141 to find the average variation for all the storms. By multiple-epoch, we mean that we have
 142 analysed the initial, main and recovery phases of the storm independently. This is the first
 143 reported study to employ a superposed epoch analysis to investigate the eigenfrequencies
 144 in cross-phase spectra. The superposed epoch analysis also puts all of the storms onto a
 145 common time grid so we can see how the average eigenfrequency varies relative to the
 146 storm phase and it prevents data from different storm phases being mixed together. By
 147 only including data in the analysis from a given MLT sector, the diurnal variation can
 148 be removed from the average. Different MLT sectors can then be analysed separately. A
 149 chain of magnetometer stations allows us to investigate changes in eigenfrequency for dif-
 150 ferent latitudes as well as magnetic local times (MLTs).

151 Previous studies have provided a valuable understanding of how mass density changes.
 152 However, due to varying instrument coverage between studies, differing techniques, and
 153 limitations of the methodology as discussed earlier, the typical storm time variations are
 154 inconclusive with reports of both enhanced mass density and depletions of mass density
 155 during geomagnetic storms. We use our data to determine whether the plasma mass den-
 156 sity increases or decreases for the average geomagnetic storm by solving the wave equa-
 157 tion of *Singer et al.* [1981] in conjunction with the TS05 magnetic field model [*Tsyga-*
 158 *nenko and Sitnov*, 2005]. It is found that whether the plasma mass density increases or
 159 decreases depends on the L-shell observed.

160 **2 Data**

161 **2.1 Geomagnetic Storm Intervals**

162 To study the average changes in eigenfrequencies during geomagnetic storms, we
 163 have used a storm list created using the method of *Walach and Grocott* [2019]. Their al-
 164 gorithm provides times which mark the four boundaries associated with the three phases
 165 mentioned in section 1: initial, main and recovery.



183 **Figure 1.** Illustration of the Sym-H algorithm on a storm from March 2002. The red section is the ini-
 184 tial phase of the storm, the blue section is the main phase and the green section is the recovery phase. An
 185 additional 12 hours of data have been shown in grey at either end of the storm interval.

166 This algorithm searches the Sym-H index for minima less than -80 nT. This is the
 167 same criteria employed by *Hutchinson et al.* [2011]. Some weak storms may have a Sym-
 168 H minimum greater than -80 nT but it was deemed best to remove these to ensure that the
 169 minimum was due to a geomagnetic storm. This minimum defines the time at the end of
 170 the main phase. An example of this procedure is illustrated in Figure 1. The beginning
 171 of the main phase is defined as the most recent time before the Sym-H minimum crossed
 172 the quiet time level of -15 nT. *Walach and Grocott* [2019] found this was a more reliable
 173 definition than using the preceding maximum Sym-H value. To define the beginning of
 174 the initial phase, the maximum value of Sym-H before the beginning of the main phase
 175 is identified. The most recent time before this when Sym-H is -15 nT is the beginning of
 176 the initial phase. Note this definition of the start of the initial phase is different to that
 177 of *Hutchinson et al.* [2011] and *Murphy et al.* [2018], who use a definition based on dy-
 178 namic pressure enhancements. The end of the recovery phase is defined as the next time
 179 after the end of the main phase when the Sym-H index returns to -15 nT. This algorithm
 180 is also discussed in *Walach and Grocott* [2019], where the list is used to investigate ge-
 181 o-magnetic storms with the Super Dual Auroral Radar Network [*Greenwald et al.*, 1995;
 182 *Chisham et al.*, 2007] from 2010 to 2016.

186 This algorithm was applied to Sym-H data from 2002 to the end of 2018. After vi-
 187 sually checking for false detections, this gave a list of 132 storms. The dates and Sym-H
 188 minima associated with each storm are given in the supplementary material.

189 2.2 Magnetometer Data

190 This study used 10 second resolution magnetometer data from the International
 191 Monitor for Auroral and Geomagnetic Effects (IMAGE) array [Luhr, 1994]. North-south
 192 component data from the stations listed in table 1 were used in the analysis, which corre-
 193 sponds to the toroidal mode if we assume a 90 degree rotation of the wave ellipse by the
 194 ionosphere [Hughes and Southwood, 1976]. Midpoint dipolar L-shell values are given to
 195 help visualise the latitudinal coverage of the pairs used in this study.

196 **Table 1.** Locations of the magnetometer pairs. Magnetic coordinates and dipolar L-shells are based on
 197 positions in 2001 - see <http://space.fmi.fi/image/www/index.php?page=stations>. These values
 198 vary slightly across the time range of the study.

Magnetometers	Identity Code	Midpoint Geo Lat.	Midpoint Geo Lon.	Midpoint CGM Lat.	Midpoint CGM Lon.	L-shell
Masi-Sørøya	MAS-SOR	68.50	22.96	66.76	106.30	6.42
Ivalo-Kevo	IVA-KEV	69.16	27.15	65.71	108.91	5.91
Pello-Muonio	PEL-MUO	67.46	23.81	64.14	105.07	5.25
Oulujärvi-Pello	OUJ-PEL	65.71	25.66	62.27	105.53	4.62
Hankasalmi-Oulujärvi	HAN-OUJ	63.39	26.92	59.84	105.34	3.96
Tartu-Nurmijärvi	TAR-NUR	59.38	25.56	55.68	102.54	3.15

199 3 Cross-Phase Superposed Epoch Analysis

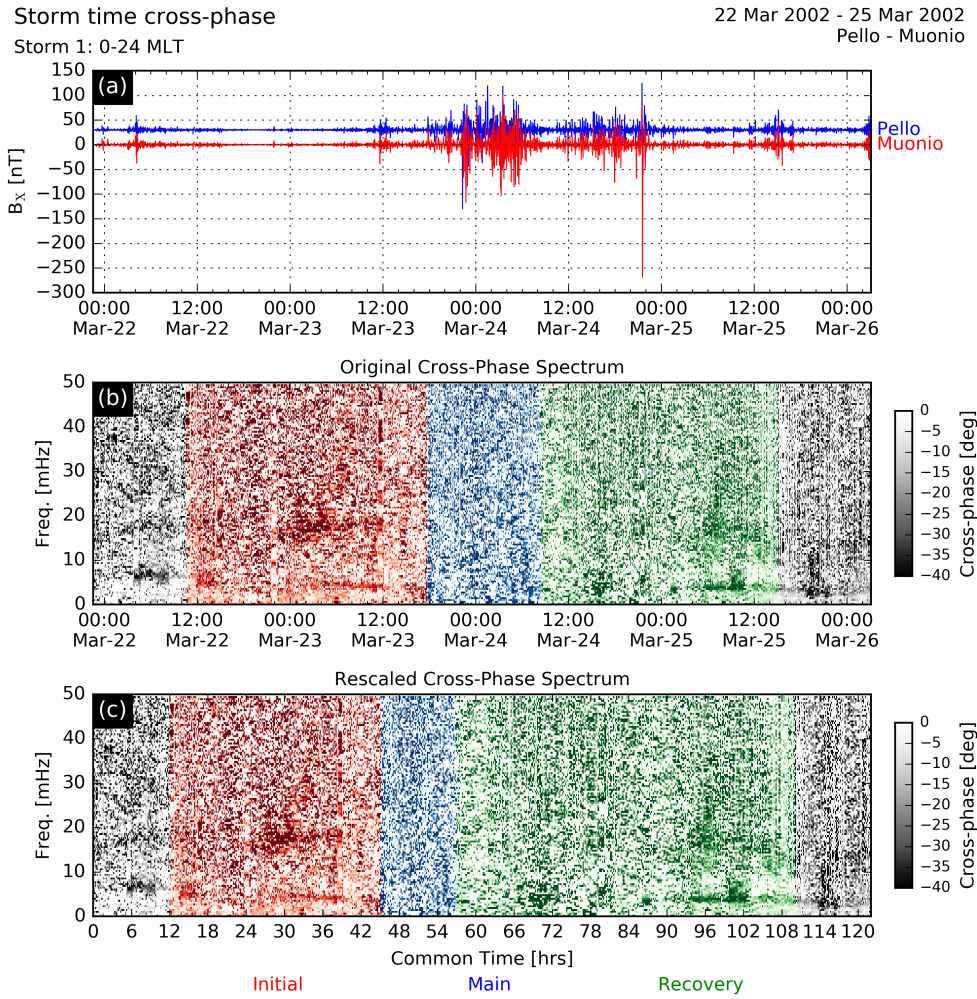
200 To investigate how the eigenfrequencies of magnetic field lines change during ge-
 201 omagnetic storms, a different approach was used to that of Wharton *et al.* [2019a]. They
 202 simply binned measurements according to their Sym-H value. However, the Sym-H index
 203 only reaches storm levels, here defined as Sym-H < -80 nT, for a very small fraction of
 204 the total time available. Data from both the main and recovery phases will also be com-
 205 bined together and no information about how the eigenfrequencies evolve with time will
 206 be available. Therefore, we have taken a different approach by applying a superposed

207 multiple-epoch analysis to the cross-phase spectra taken during the storm intervals iden-
208 tified with the method of *Walach and Grocott* [2019] described in section 2.

209 The eigenfrequencies were determined using the cross-phase technique of *Waters*
210 *et al.* [1991], which requires two latitudinally and closely spaced ground-based magne-
211 tometers. Two are required to detect the phase change with latitude that occurs at the res-
212 onant frequency of the midpoint of the magnetometers. Several papers have automated
213 this technique [*Berube et al.*, 2003; *Chi et al.*, 2013; *Sandhu et al.*, 2018b; *Wharton et al.*,
214 2018].

215 Further to this, *Wharton et al.* [2019b] developed a Lomb-Scargle (LS) cross-phase
216 technique that could process unevenly spaced data and use a higher frequency resolution
217 because the frequency grid is independent of the properties of the data used. The cho-
218 sen resolution was 4 times that achievable with a discrete fourier transform as this value
219 was adopted in previous studies which used LS [e.g., *Bland et al.*, 2014; *Wharton et al.*,
220 2019b,a]. The dynamic cross-phase spectrum uses a 40 minute sliding window, which
221 gives a frequency resolution of 0.417 mHz without oversampling for the IMAGE mag-
222 netometer resolution. Changing the oversampling factor to 4 reduces the frequency res-
223 olution to 0.104 mHz, allowing us to be more precise in determining the frequencies of
224 waves. The LS technique is not intrinsically more accurate than using the Discrete Fourier
225 Transform, but it does allow us to create a denser frequency axis. This was the motiva-
226 tion for using it in this paper.

227 The superposed multiple-epoch analysis method used by *Hutchinson et al.* [2011]
228 was then applied to the derived cross-phase spectra. This method treats the three phases
229 of geomagnetic storms separately by calculating the mean duration of each of the three
230 storm phases (initial, main and recovery). A superposed epoch analysis is then applied
231 to each storm phase. This method is better than applying a superposed epoch analysis to
232 the whole storm interval because the durations of each phase are not always in the same
233 proportion to each other for different storms. Treating the three phases independently ac-
234 counts for this. These mean durations were 33.16, 11.76 and 53.10 hours for the initial,
235 main and recovery phases, respectively. This enabled us to create a common time grid to
236 which the three phases of each storm could be normalised to so we could observe average
237 changes in each of the three storm phases.



238 **Figure 2.** Rescaling of cross-phase spectra. (a) Boxcar filtered magnetometer data for the two stations.
 239 (b) Original LS cross-phase spectrum. Initial phase - red. Main phase - blue. Recovery phase - green. (c)
 240 Cross-phase spectrum rescaled to the common time axis using the method of *Hutchinson et al.* [2011].

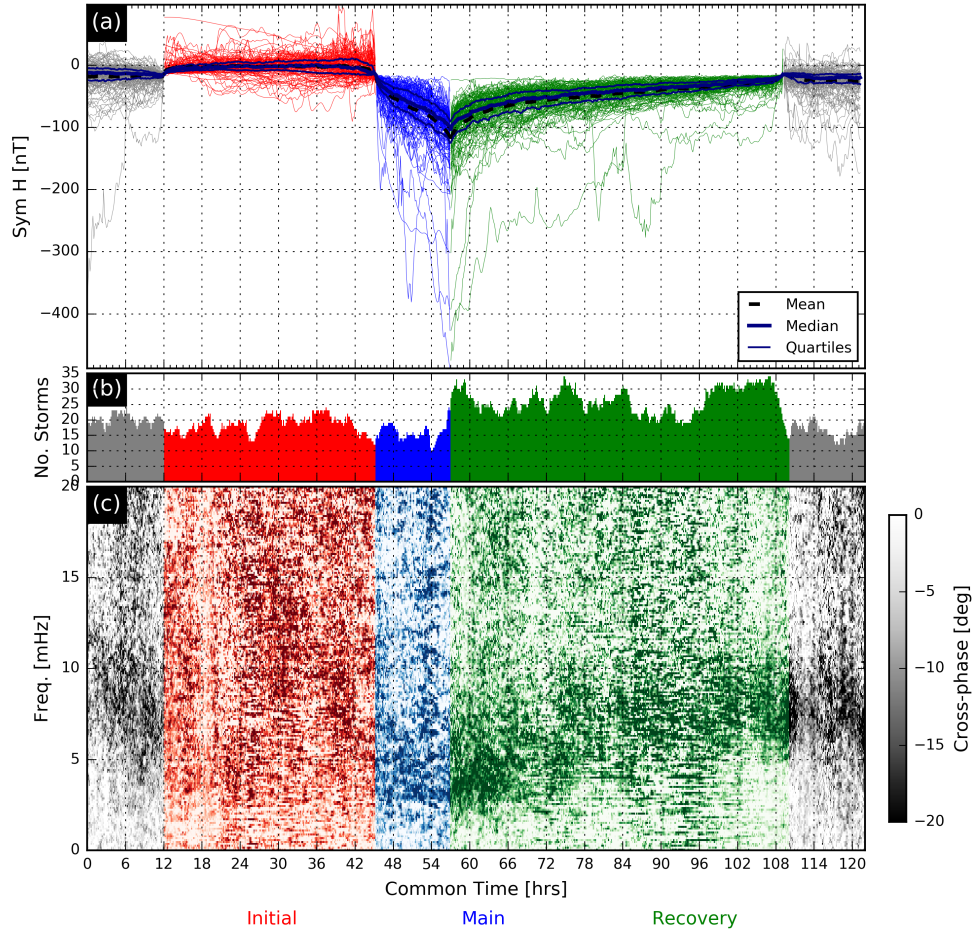
241 For each storm, the LS cross-phase spectrum was calculated. Figure 2 shows an ex-
242 ample of how the rescaling was performed on one of the storm intervals. Figure 2a con-
243 tains the filtered magnetometer data (800 second boxcar filter [Wharton *et al.*, 2018]) for
244 two magnetometer stations. Figure 2b shows the LS cross-phase spectrum for this storm.
245 The initial, main and recovery phases have been shaded red, blue and green, respectively.
246 An additional 12 hours of data has been included on each end, shaded in grey, to repre-
247 sent the quiet time periods, and will be used to compare variations to quiet time condi-
248 tions.

249 Before the rescaling and averaging process could be performed, there is a complica-
250 tion concerned with MLT that had to be considered. The full duration of a geomagnetic
251 storm is usually a few days. This means that the diurnal variation of the eigenfrequencies
252 must be taken into account. For example, eigenfrequencies are always higher in the morn-
253 ing sector than the afternoon [e.g., Takahashi *et al.*, 2016; Wharton *et al.*, 2018]. This is
254 because the plasma mass density is higher in the afternoon sector relative to the morning
255 due to flux tubes refilling from the ionosphere throughout the day. If this is not accounted
256 for, changes in the eigenfrequencies that are diurnal and storm related will be mixed to-
257 gether. To compensate for this, a MLT sector is first defined (e.g. 10-14). We arbitrarily
258 chose 4 hours as a compromise between minimising diurnal variability and not exclud-
259 ing too much data. Only data taken when the magnetometer pair were within that MLT
260 sector were included in the superposed epoch analysis described above. The analysis was
261 then performed independently for other MLT sectors. This minimised contamination of the
262 spectra by diurnal variation so that only the storm-related variations were observed.

263 To perform the superposed epoch analysis, each frequency in the periodogram was
264 treated as its own time series. Each "frequency time series" was interpolated and then
265 rescaled to the common time axis for each phase of the storm. This gave the rescaled LS
266 cross-phase spectrum in Figure 2c. This process was repeated for all storms so that the
267 spectra could then be superposed and averaged using the common time grid. In this exam-
268 ple, data from all 24 hours of MLT have been included to more clearly show the rescal-
269 ing process. For the forthcoming analysis, only data taken from 4-hour MLT sectors is
270 included. The equivalent plot here would contain considerable white space due to the ex-
271 cluded data.

Average storm time cross-phase: 10-14 MLT

132 storms
 PEL - MUO: L = 5.21



272 **Figure 3.** Superposed multiple-epoch analysis results for the Pello-Muonio station pair in the 10-14 MLT
 273 window. (a) Superposed multiple-epoch analysis on the Sym-H data. The dashed line shows the mean Sym-H
 274 value, the thick solid line shows the median and the thin solid lines show the upper and lower quartiles. (b)
 275 The number of storms contributing to the average as a function of common time. (c) Superposed multiple-
 276 epoch analysis of the LS cross-phase spectra. Red shading indicates initial phase, blue is main phase and
 277 green is recovery phase. Grey is 12 hours before and after the storm.

278 The superposed multiple-epoch analysis method used by *Hutchinson et al.* [2011]
 279 was also applied to variables from the OMNI dataset, which describes the upstream solar
 280 wind and contains geomagnetic indices. This is shown for the Sym-H index in Figure
 281 3a, where the three phases of the storm have the same colour (red, blue and green). The
 282 mean, median, upper and lower quartiles of the Sym-H index have been overplotted.

283 Figure 3 gives an example of the superposed epoch analysis applied to the 132 storms
 284 for the Pello-Muonio magnetometer pair in the 10-14 MLT sector. Figure 3b shows the
 285 number of storms which contributed data to each time on the common time axis. This
 286 number varies because the storms were not equally distributed in MLT. On average, 22
 287 storms were expected at any given time due to the size of the MLT sector.

288 Figure 3c shows the results of the superposed epoch analysis on the LS cross-phase
 289 spectra taken in the 10-14 MLT sector for all 132 storms. The LS cross-phase spectra
 290 for all of the storms have been circularly averaged in each frequency - common time bin
 291 because the cross-phase is a circularly distributed variable [*Mardia and Jupp, 2000*]. A
 292 variation in the fundamental eigenfrequency is visible. The trend is least clear in the ini-
 293 tial phase but begins at ~ 8 mHz at the beginning of the phase and reaches ~ 4 mHz at
 294 the start of the main phase. Other bands can also be seen at higher frequencies, which
 295 complicates the interpretation of the harmonic numbers. The eigenfrequency reaches a
 296 minimum at ~ 4 mHz in the main phase, where it remains steady before increasing again
 297 throughout the recovery phase back to 8 mHz. Only the fundamental was observable in
 298 the recovery phase.

299 Identifying the fundamental eigenfrequency in the initial phase is ambiguous and
 300 complicated by the possible presence of a higher harmonic. This could be the third har-
 301 monic, based on the arguments in *Wharton et al.* [2018], and it also decreases in value to-
 302 wards the main phase from ~ 15 mHz to ~ 5 mHz. It could also be the fundamental eigen-
 303 frequency increasing around 24 hours then decreasing again. The selection algorithm in
 304 section 4.1 tries to address this ambiguity with a manual process.

305 The same analysis was performed for the other station pairs at the latitudes given in
 306 Table 1. Although there were some differences in whether the third or fundamental har-
 307 monic were being observed during the initial phase, a consistent pattern of decreasing
 308 eigenfrequencies was observed at all but the lowest latitudes. This decrease in eigenfre-
 309 quency with increasingly negative Sym-H is in agreement with observations by *Sandhu*

310 *et al.* [2018a] and *Wharton et al.* [2019a]. Other latitudes and MLTs are presented in the
 311 next section, and the results will be summarised in Figures 6 and 7, which separate out
 312 the storm time and diurnal variation.

313 **4 Controlling Factors for the Eigenfrequency**

314 Changes in the eigenfrequency values depend on the magnetic field structure and
 315 plasma mass density, as discussed in section 1. Calculating the average changes in these
 316 parameters allows an understanding of why the eigenfrequencies vary throughout the storm
 317 cycle. To do this, a range of appropriate frequencies centred on the eigenfrequency must
 318 be extracted from the data and expressed as a function of the common time axis to enable
 319 calculation. This is difficult using the data in the format displayed in Figure 3. Section 4.1
 320 describes this extraction process. In section 4.2, we parameterise the TS05 magnetic field
 321 model [*Tsyganenko and Sitnov, 2005*] and calculate the plasma mass density. In section
 322 4.3, we repeat this for all station pairs in Table 1 and for a range of MLTs. This enables
 323 the derivation of eigenfrequency maps and, by accounting for magnetic field changes ac-
 324 cording to the TS05 model, estimations of equatorial plasma mass density. The results
 325 provide a fuller understanding of how the structure of the dayside magnetosphere changes
 326 during geomagnetic storms, at least within the region covered by the magnetometers in
 327 this study.

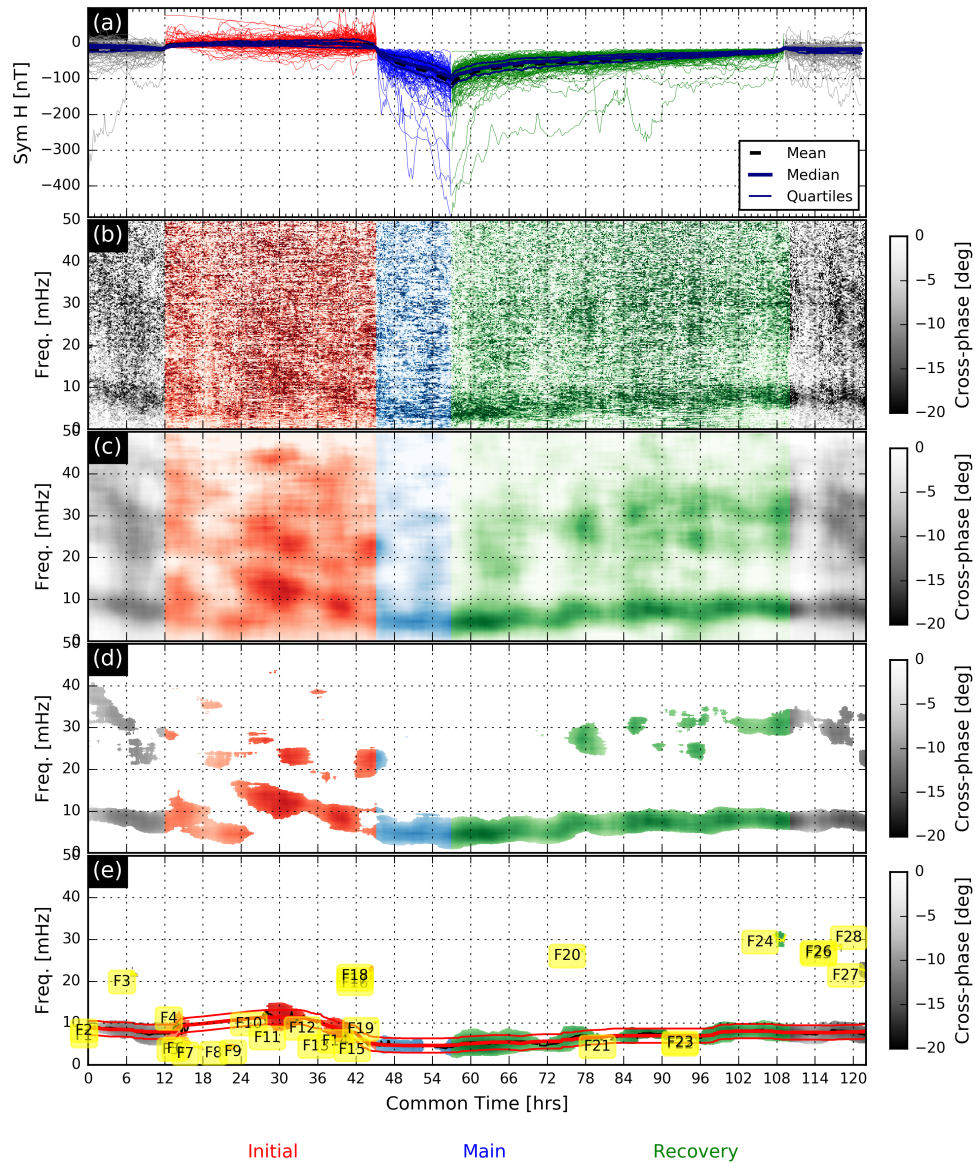
328 **4.1 Isolating the Fundamental Eigenfrequency**

329 The technique to extract the fundamental eigenfrequency profile is based on that
 330 of *Wharton et al.* [2018] with an additional step, which is illustrated in Figure 4. Fig-
 331 ures 4a and 4b are reproduced directly from Figure 3. The LS cross-phase spectrum is
 332 first smoothed in both time and frequency (Figure 4c). To do this for any given value,
 333 it is averaged with values within ± 2 mHz and ± 2 hours, giving a range or box size of 4
 334 mHz by 4 hours. At the edges of the spectrum, these ranges will be capped by the spec-
 335 trum boundaries (0 or 50 mHz for frequency and the start and end times), shrinking these
 336 ranges to half their size for the boundary values. Hence, the standard error will be larger
 at the plot boundaries. The standard deviation is also calculated and stored for the pur-
 poses of the *t*-test explained below.

Average storm time cross-phase: 10-14 MLT

132 storms
Pello - Muonio

Averaging Box: 4.0 mHz - 4.0 hrs



329 **Figure 4.** Procedure for isolating the fundamental frequency. (a) Superposed epoch analysis results on
 330 the Sym-H index data. (b) Average LS cross-phase spectrum. (c) Smoothed, average LS cross-phase spec-
 331 trum. (d) Smoothed spectrum after column test. Only values less than the column mean minus one standard
 332 deviation are kept. (e) Spectrum after the t -test. Only cross-phase values with a t -statistic greater than 1
 333 remain. Each independent feature is identified and labelled (yellow). "F" stands for feature and the number
 334 corresponds to the order in which they were identified. Features thought to contribute to the fundamental are
 335 selected and a line is fitted through them and smoothed (thick red line). Thin red lines indicate the uncertainty
 336 in the eigenfrequency described in the text.

347 Next, the mean and standard deviation of the cross-phase for each common time
348 are calculated. Only values less than the mean minus one standard deviation are retained.
349 The result of this is illustrated in Figure 4d. It can be seen that a narrow frequency band
350 where the fundamental frequency lies dominates the remaining data. Then a t -test is ap-
351 plied to remove the non-resonant features. The statistic is the smoothed cross-phase value
352 divided by its standard deviation and multiplied by minus 1. Only cross-phase values with
353 a t statistic greater than one are kept. Non-resonant signatures randomly had a highly neg-
354 ative cross-phase value, but their large standard deviation can be used to remove them.
355 Only the stable values then remain, which are presumed to represent real eigenfrequen-
356 cies. This process is also discussed in *Berube et al.* [2003], the algorithm upon which the
357 *Wharton et al.* [2018] algorithm was originally based. These are shown in Figure 4e.

358 We then use a process that searches through the spectrum and isolates the remaining
359 independent features and assigns them a number. This process searches up each column
360 in Figure 4d, beginning at the bottom left, until it finds a data point. It then searches this
361 column and adjacent columns for data in adjacent cells and groups this data together. This
362 group is a feature and this data is then discounted from the rest of the search. Once all
363 points that are grouped together are found, the search up the columns continues looking
364 for the start of the next feature and so forth. The final list of identified features are la-
365 belled with the numbers in the yellow boxes in Figure 4e that are automatically attached
366 to their respective features. "F" stands for feature and the number corresponds to the order
367 in which they were identified. Hence, lower numbers are to the left where the search be-
368 gan. The user can then manually select which "features" they think contribute to the fun-
369 damental eigenfrequency. This is a subjective process to a certain extent. In some cases,
370 the labels overlap because two features begin in very similar locations on the plot. In such
371 circumstances, trial and error is unfortunately required to select the desired features. For
372 the example in Figure 4e, the features 1, 2, 10, 12, 15, 21, 22 and 23 were selected by the
373 user. These features are then fitted with a smooth line to yield an eigenfrequency profile,
374 which is the thick red line in Figure 4e.

375 The band identified in Figure 4e is spread over a range of frequencies. An uncer-
376 tainty on the eigenfrequency is found by calculating the mean frequency width of the se-
377 lected features that composed the fundamental eigenfrequency. This range is illustrated by
378 the two thin red lines in Figure 4e and represents an estimate in the uncertainty in measur-
379 ing the fundamental frequency using this method.

380 This method was considered more reliable than employing a complicated automated
 381 algorithm. The primary issue is that there are often multiple harmonics which could con-
 382 taminate the fundamental, so automatic identification becomes difficult. This method was
 383 a way of resolving this problem. It is noted that advanced machine learning methods
 384 could be applied in future but such methods were not needed for the small number of
 385 cases in this study.

386 4.2 Determining the Plasma Mass Density

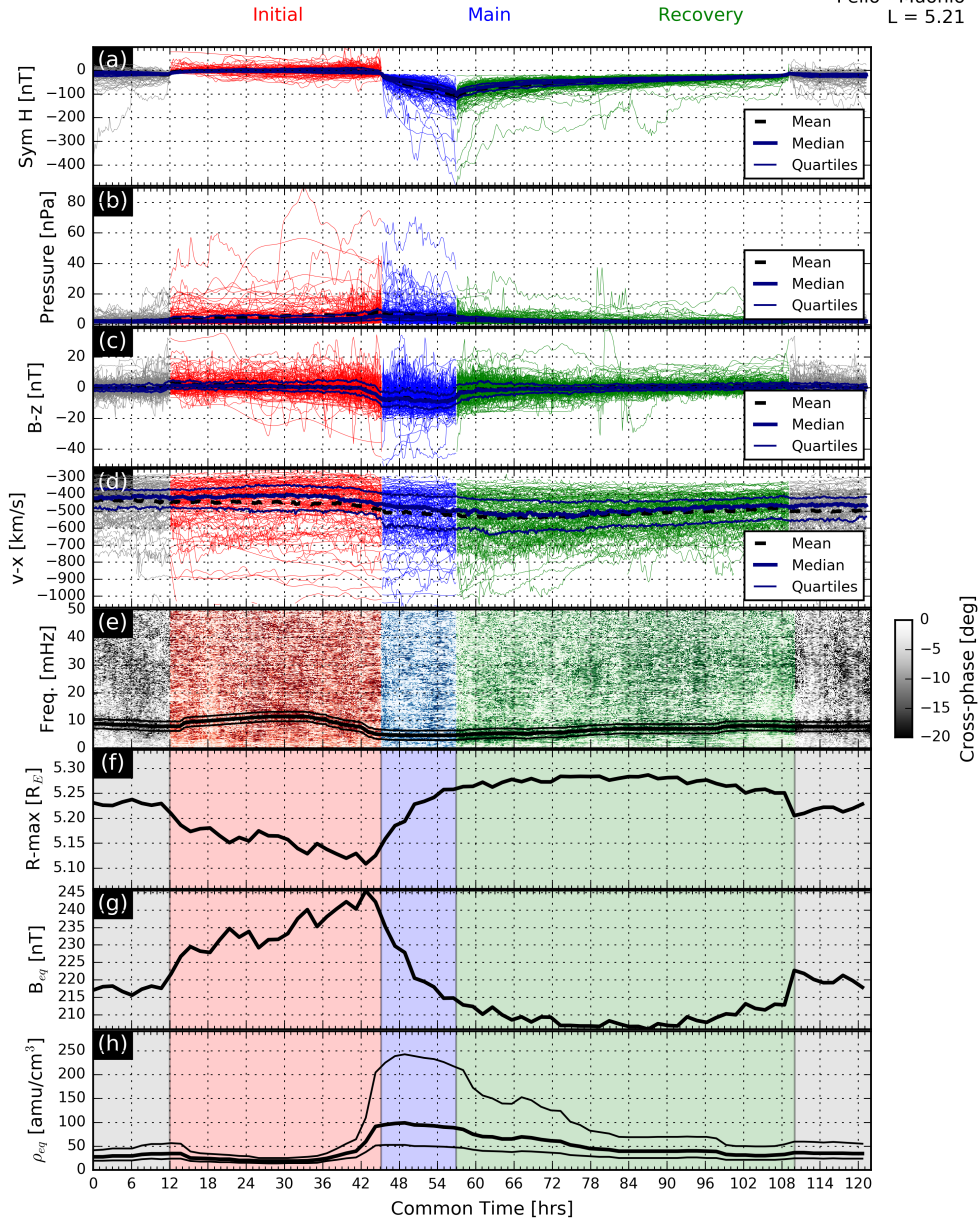
387 Once the fundamental frequency has been determined as a function of the common
 388 time as described in section 4.1, the next step is to describe the magnetic field line. Once
 389 achieved, the magnetohydrodynamic wave equation of *Singer et al.* [1981], equation (2),
 390 can be solved to determine the plasma mass density.

391 We chose the TS05 magnetic field model [*Tsyganenko and Sitnov, 2005*] to model
 392 the magnetic field lines, which was designed to include the variability introduced by geo-
 393 magnetic storms and specifically includes a ring current contribution. *Huang et al.* [2008]
 394 have shown that the performance of this model is better than previous empirical magnetic
 395 field models. The parameters for this model are the Dst index (we have used the Sym-
 396 H index, which can be considered as a high resolution Dst index [*Wanliss and Showal-*
 397 *ter, 2006*]), solar wind dynamic pressure and velocity, IMF x and y components and the
 398 dipole tilt angle.

406 To parameterise the TS05 model across the common time axis, the superposed multiple-
 407 epoch analysis method described in section 3 was applied to the Sym-H, pressure, IMF B_z
 408 and solar wind velocity x -component data. This process is illustrated in Figure 5 for the
 409 Pello-Muonio pair in the 10-14 MLT sector. The superposed epoch analysis of the Sym-
 410 H, dynamic pressure, IMF B_z and solar wind velocity x -component data are shown in
 411 Figure 5a-d. The mean values of these four parameters at each common time were used
 412 for parameterising the TS05 model. The solar wind velocity y and z components, dipole
 413 tilt angle and IMF B_y data were all set to zero, as this was their expected average values.
 414 Over long time scales, the solar wind flow is expected to be radial and the dipole tilt an-
 415 gle will average to zero. Therefore, the IMF B_y component should not affect the storm
 416 process either. This was confirmed from applying the superposed epoch analysis method

Average storm time cross-phase: 10-14 MLT

132 storms
Pello - Muonio
L = 5.21



399 **Figure 5.** Process to retrieve magnetic field and plasma mass density information. Superposed multiple-
 400 epoch analyses for (a) Sym-H index, (b) solar wind dynamic pressure, (c) IMF B_z component and (d) solar
 401 wind velocity v_x component. (e) Superposed epoch analysis LS cross-phase spectrum with fundamental
 402 eigenfrequency profile overplotted. (f) Radial position of the magnetic field line for this magnetometer pair
 403 according to the TS05 model. (g) Equatorial magnetic field strength. (h) Equatorial plasma mass density.
 404 The thicker line is for the middle eigenfrequency profile, thinner lines correspond to the upper and lower
 405 eigenfrequency bounds.

417 to these variables to check. The superposed epoch analysis cross spectrum from Figure 3b
 418 is reproduced in Figure 5e with the eigenfrequency profile from Figure 4e plotted over it.

419 The TS05 model was evaluated for every tenth point available on the common time
 420 axis. Figure 5f shows the maximum radial distance of any point along the field line, as-
 421 sumed to represent the equatorial crossing point. As the initial phase begins, the field line
 422 moves earthward until the main phase, where it then moves outwards beyond its original
 423 position. The field lines recover towards their original position at the end of the recovery
 424 phase.

425 Plotted in Figure 5g is the magnetic field strength at the maximum radial distance
 426 of the field line. Note that in the equatorial plane, the magnetic field strength is primarily
 427 dominated by the B_z component. This is observed to increase throughout the initial phase
 428 as the magnetopause currents are enhanced and the closed magnetic field line strength in-
 429 creases, then drops throughout the main phase as the enhanced ring current weakens the
 430 background magnetic field. It then returns to normal during the recovery phase. These re-
 431 sults show that the TS05 model is capturing the expected aspects of a geomagnetic storm.

432 The MHD wave equation, derived by *Singer et al.* [1981],

$$\frac{d^2}{ds^2} \left(\frac{\epsilon_\alpha}{h_\alpha} \right) + \frac{d}{ds} \left(\ln \left(h_\alpha^2 B_0 \right) \right) \frac{d}{ds} \left(\frac{\epsilon_\alpha}{h_\alpha} \right) + \frac{\mu_0 \rho \omega^2}{B_0^2} \left(\frac{\epsilon_\alpha}{h_\alpha} \right) = 0 \quad (2)$$

433 has been used to calculate the equatorial plasma mass density. The justification for
 434 using this equation is given below. Solving this equation requires knowledge of the mag-
 435 netic field structure and the eigenfrequency. We have used the TS05 magnetic field model
 436 and the eigenfrequencies measured from our data. In equation (2), ϵ_α is the field line
 437 displacement, h_α is a scaling factor describing the separation of the field lines along the
 438 field, s is the field-aligned coordinate, B_0 is the ambient magnetic field strength, μ_0 is the
 439 magnetic permeability of free space, ω is the angular eigenfrequency and ρ is the plasma
 440 mass density. The separation h_α is calculated in the toroidal direction using a closely
 441 spaced field line.

442 *Singer et al.* [1981] state that equation (2) can be applied to any arbitrary geome-
 443 try. The derivation of this equation implicitly assumes that orthogonal field-aligned co-
 444 ordinates can be used. However, *Salat and Tataronis* [2000] have shown that such fields
 445 only exist in special cases, such as a dipolar field. In general, fields that can support field

446 aligned orthogonal coordinates do not exist and this includes the TS05 fields. Using or-
 447 thogonal coordinates requires $\mathbf{B} \cdot (\nabla \times \mathbf{B}) = 0$, or that there is no shear in the magnetic
 448 field. An absence of shear requires that the magnetic field is zero in one of the three co-
 449 ordinate directions. In a dipole field, this would be the azimuthal direction. For a more
 450 realistic magnetospheric field line, there will be variation in the magnetic field in all three
 451 field-aligned coordinates due to shear and thus an orthogonal field aligned coordinate sys-
 452 tem is not possible. Therefore, solving the wave equation in a non-orthogonal coordinate
 453 system such as that of *Rankin et al.* [2006] would be more accurate, despite the more com-
 454 plicated formulation of the wave equation. In this study though, we only consider mag-
 455 netic field lines in the dayside magnetosphere away from the magnetopause, which can be
 456 considered to be quasi-dipolar. Hence, any error from using equation (2) is expected to be
 457 minimal, and many other authors have used this equation when tackling this problem [e.g.,
 458 *Waters et al.*, 1996; *Berube et al.*, 2006; *Wharton et al.*, 2018]. Therefore, we have applied
 459 this equation to our problem.

460 Equation (2) is solved using the Runge-Kutta method described in *Wharton et al.*
 461 [2018]. The plasma mass density is assumed to have the power law form for its distribu-
 462 tion along the field line given by

$$\rho = \rho_{eq} \left(\frac{r_{eq}}{r} \right)^3 \quad (3)$$

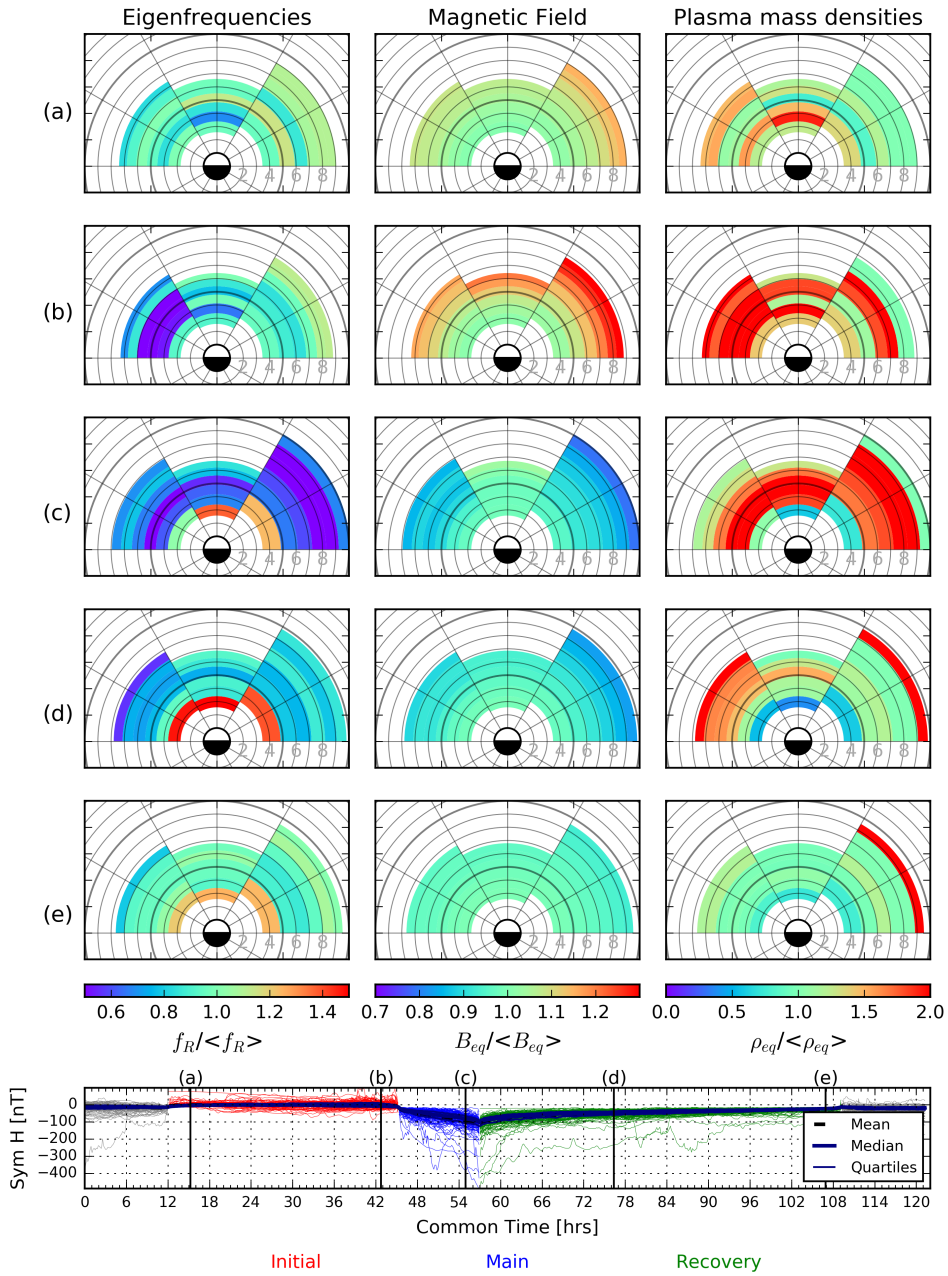
463 This is a common assumption made by many authors [e.g., *Angerami and Thomas*,
 464 1964; *Carpenter and Smith*, 1964; *Cummings et al.*, 1969; *Orr and Matthew*, 1971; *Menk*
 465 *et al.*, 1999, 2004; *Denton et al.*, 2006; *Wharton et al.*, 2018]. In equation 3, ρ is the plasma
 466 mass density and r is the radial position along the field line. The subscript eq represents
 467 the equatorial value. The exponent determines the rate at which the plasma mass density
 468 changes with radial distance. A positive exponent causes the plasma mass density to de-
 469 crease radially, so that it reaches a minimum along a field line in the equatorial plane. An
 470 exponent of 3 has been used and it is assumed this is a reasonable value based on other
 471 studies and has been used by many other authors [e.g., *Poulter et al.*, 1984; *Menk et al.*,
 472 1999, 2004]. This distribution contains a minimum at the equator and maxima at the base
 473 of the field lines in the ionosphere. The size of this exponent has been shown to make
 474 little difference to the calculated equatorial mass densities [e.g., *Orr and Matthew*, 1971;
 475 *Menk and Waters*, 2013].

476 The equatorial plasma mass density profiles calculated with the mean fundamen-
 477 tal frequency and the upper and lower bounds are shown in Figure 5h. The lower bound
 478 eigenfrequency corresponds to the highest plasma density and vice versa. In this example,
 479 the plasma density remains stable throughout the initial phase, which could suggest that as
 480 the magnetosphere is compressed, that plasma loss processes increase. The plasma mass
 481 density then increases to its highest value at the beginning of the main phase. It then de-
 482 creases back to quiet time levels throughout the recovery phase. Small differences in the
 483 eigenfrequency correspond to large differences in the calculated plasma mass densities, in
 484 agreement with previous studies [e.g., *Takahashi and Denton, 2007*].

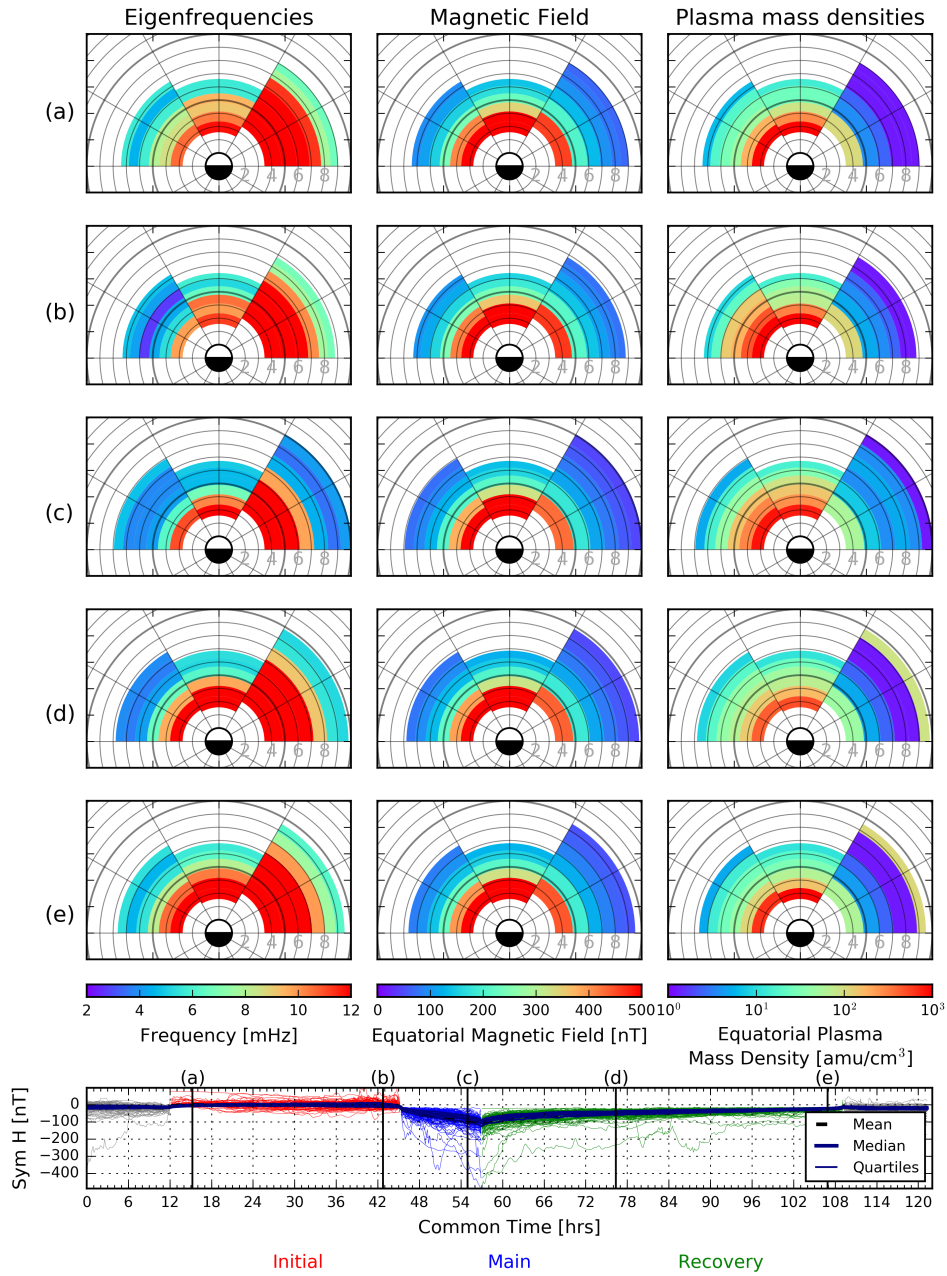
485 **4.3 Mapping the Plasma Mass Density**

486 The process of estimating the equatorial mass density described in section 4.2 was
 487 repeated for each station pair in Table 1 for three MLT sectors, 6-10 MLT, 10-14 MLT
 488 and 14-18 MLT. Only the dayside was considered because the cross-phase technique is
 489 ineffective at night [e.g., *Wharton et al., 2019a*]. There was considerable variation in the
 490 plasma mass density profiles between different stations and MLTs. These results have been
 491 summarised by the maps in Figure 6, similar to those created in *Corpo et al. [2018]* using
 492 data from the European Meridional Magnetometer Array and parameterised by Kp index.
 493 The fundamental eigenfrequency measured with the LS cross-phase technique in section
 494 4.1, the modelled equatorial magnetic field strength from the TS05 model and the inferred
 495 equatorial plasma mass densities, both from section 4.2, are shown for each radial posi-
 496 tion and MLT sector for five intervals along the common time axis. These five times are
 497 labelled (a) to (e) and are indicated on the Sym-H index plot at the bottom. The TS05
 498 model was used to map the field line of each station pair to the equatorial plane for each
 499 point in time, which accounts for the variation in field line length as the storms progress.
 500 The eigenfrequency data are shown on the left, equatorial magnetic field data in the mid-
 501 dle and equatorial plasma mass density data on the right. Plots of the form of Figure 3
 502 show that there are a sufficient number of storms in each MLT sector at all times to do
 503 this analysis.

513 For each MLT-radial bin, the quiet time average value of either the eigenfrequency,
 514 magnetic field strength or plasma mass density is calculated from the 12 hour period be-
 515 fore the initial phase and the 12 hour period after the recovery phase. These data are
 516 shaded in grey in Figures 1-5. This value is then used to normalise the respective data



504 **Figure 6.** Variations of measured eigenfrequencies, modelled equatorial magnetic field strengths and
 505 calculated equatorial plasma mass densities relative to the local quiet time averages. Left column: eigenfre-
 506 quencies. Middle column: magnetic field strength. Right column: plasma mass densities. Each row shows the
 507 magnetospheric state at five intervals during the average geomagnetic storm, marked on the Sym-H index plot
 508 at the bottom.



509 **Figure 7.** Absolute variations of eigenfrequencies, equatorial magnetic field strengths and equatorial
 510 plasma mass densities. Left column: eigenfrequencies. Middle column: magnetic field strength. Right col-
 511 umn: plasma mass densities. Each row shows the magnetospheric state at five intervals during the average
 512 geomagnetic storm, marked on the Sym-H index plot at the bottom.

517 in that bin so we can see how the values change relative to their quiet time average. This
 518 approach made it much easier to discern the general trends as opposed to observing indi-

519 vidual plots such as Figure 5. Each colour scale is centered on 1. Hence, blue indicates a
 520 reduction in that value and red an increase relative to quiet times.

521 An equivalent plot with absolute eigenfrequency, equatorial magnetic field and plasma
 522 mass density values is shown in Figure 7 in the same format as Figure 6. This shows that
 523 the variation in eigenfrequency with L-shell and MLT is much greater than the storm time
 524 variation at any given position, making such variations difficult to discern. Hence, we fo-
 525 cuse our discussion on the normalised data in Figure 6. Here, an L value refers to the ra-
 526 dial distance in the equatorial plane to the field line in Earth radii.

527 Row (a) of Figure 6 shows the beginning of the initial phase, when values are near
 528 the quiet time average. Row (b) shows the end of the initial phase, where the eigenfre-
 529 quencies have decreased in the 14-18 MLT sector and the magnetic field strength has in-
 530 creased for the outer L-shells. There has also been an increase in the plasma mass density,
 531 mostly clearly in the afternoon sector.

532 Row (c) of Figure 6 shows the end of the main phase. The eigenfrequencies have
 533 decreased by as much as 50% across most L-shells and MLTs. At the innermost L-shells,
 534 the eigenfrequencies are actually greater than the local quiet time average. The magnetic
 535 field has weakened, especially in the 6-10 and 14-18 MLT sectors. The plasma mass den-
 536 sity has also increased across all sectors, except at the innermost L-shells where the oppo-
 537 site is observed.

538 Row (d) of Figure 6 shows partway through the recovery phase. The eigenfrequen-
 539 cies have risen back towards mean levels again but at the innermost L-shells, they are still
 540 higher than during quiet times. The magnetic field is still weaker than during quiet times.
 541 The plasma mass density has decreased again and remains above average only at the out-
 542 ermost L-shells. It is still below average at the inner distances. Finally, row (e) shows
 543 the end of the recovery phase, where for the most part, all three parameters have returned
 544 back to their quiet time averages.

545 **5 Discussion**

546 Based upon this analysis, Figure 6 demonstrates that there is a clear pattern in the
 547 behaviour of measured toroidal eigenfrequencies during an average geomagnetic storm.
 548 The Alfvén speed, and hence a given field line eigenfrequency, is proportional to the mag-
 549 netic field strength and inversely proportional to the square root of the plasma mass den-

550 sity (equation (1)). Hence, understanding both the field line structure and the plasma mass
 551 density distribution are necessary to determine why any field line eigenfrequency changes
 552 with time.

553 Section 5.1 discusses the changes seen at $L > 4$ in the context of changing magnetic
 554 field strength and plasma mass densities. Section 5.2 then discusses changes observed for
 555 $L < 4$, which had different variations in eigenfrequency and plasma mass density.

556 **5.1 Causes of the Variation in the Eigenfrequencies: $L > 4$**

557 Figure 7 shows that during all phases of the storm, the eigenfrequencies are con-
 558 sistentlly greater in the morning sector than the afternoon sector which is the same across
 559 all observed L-shells. With asymmetries in magnetic field configuration as described by
 560 the TS05 model removed, the asymmetry persists and consequently must be caused by
 561 plasma mass density asymmetry. This asymmetry in MLT is well documented [e.g., *Poul-*
 562 *ter et al.*, 1984; *Takahashi and McPherron*, 1984; *Takahashi et al.*, 2016; *Sandhu et al.*,
 563 2018b; *Wharton et al.*, 2018, 2019a], and we confirm that this asymmetry persists through-
 564 out all phases of a geomagnetic storm. The higher plasma mass densities in the afternoon
 565 lower the Alfvén speed in this sector. This extra plasma could be due to the existence of a
 566 plasmaspheric bulge, plasmaspheric plume or increased refilling of ionospheric flux tubes.
 567 The average ion mass is also greater in the afternoon sector due to convection of heavy
 568 ions from the nightside plasma sheet [*Sandhu et al.*, 2016].

569 We now consider the storm-time variations that occur for $L > 4$. Figure 6b shows
 570 the change that occurs during the initial phase. For $L > 4$, the eigenfrequencies first de-
 571 crease in the afternoon sector which corresponds with plasma mass density increases of
 572 approximately 100% in some cells. This change is also most prevalent at $L < 7$. At radial
 573 distances greater than this, the magnetic field has increased due to the enhanced magne-
 574 topause currents, which would increase the eigenfrequencies.

575 Changes during the main phase are shown in Figure 6c. Here, the eigenfrequen-
 576 cies have decreased by as much as 50% across all MLT sectors. This corresponds with a
 577 magnetic field decrease, most prevalent away from the noon sector where magnetospheric
 578 compression is strongest, and plasma mass density increases across all MLT sectors. The
 579 decrease in eigenfrequency during the main phase when the ring current index is low

580 agrees with the observations by *Chi et al.* [2005], *Takasaki et al.* [2006], *Kale et al.* [2009],
581 *Sandhu et al.* [2018a], *Wharton et al.* [2019a] and *Rae et al.* [2019].

582 Figures 6d and 6e show that the eigenfrequencies recover back to their quiet time
583 levels as the recovery phase progresses. The return to quiet time values takes longest in
584 the afternoon sector. This may be due to the existence of a lasting plasmaspheric plume.

585 The storm-time variation in the equatorial magnetic field strength is as expected,
586 due to the increase of the ring current magnetic field. However, this study demonstrates
587 that the role of the plasma mass densities in determining the storm time evolution of the
588 eigenfrequencies is greater than previously thought by *Sandhu et al.* [2018a] and *Rae et al.*
589 [2019]. Previous studies have differed about whether the plasma mass density increases
590 or decreases during storms. *Sandhu et al.* [2017] found using an empirical model that the
591 plasma mass density decreased during intervals of low Dst index, despite the average ion
592 mass increasing. This was because the electron number density decreased due to increased
593 magnetospheric convection. Several other studies have also put forward evidence that the
594 plasma mass density decreases during enhanced geomagnetic activity [e.g., *Dent et al.*,
595 2006; *Denton et al.*, 2006; *Menk et al.*, 2014; *Corpo et al.*, 2018]. However, there are other
596 studies that have found the plasma mass density increases [e.g. *Takahashi et al.*, 2002; *Chi*
597 *et al.*, 2005; *Takasaki et al.*, 2006; *Takahashi et al.*, 2006; *Kale et al.*, 2009; *Takahashi*
598 *et al.*, 2010], which agrees with our findings. This increase was attributed to an increas-
599 ing average ion mass [e.g., *Kronberg et al.*, 2014]. We show that at distances of $L > 4$, the
600 plasma mass density doubles during the main phase of the storm across the whole dayside
601 MLT sector and a wide range of L-shells. This shows that the plasma mass density and
602 the magnetic field change in cooperation instead of opposition to lower the eigenfrequen-
603 cies.

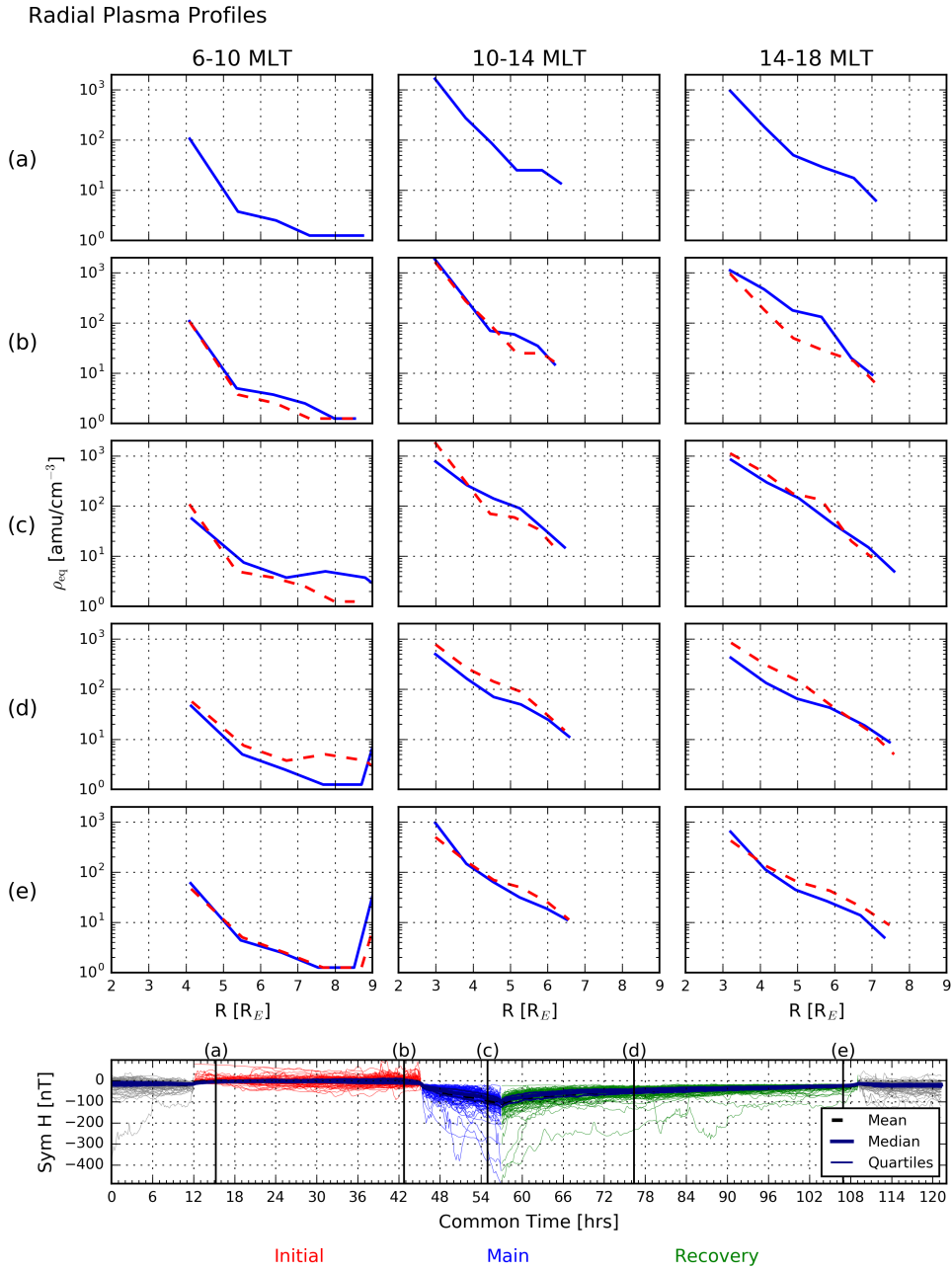
604 Where does this extra plasma mass originate from during the geomagnetic storm?
605 The density of the hot O^+ population has been shown to increase during the main phase
606 for $L < 7$ [*Yue et al.*, 2019], and the partial pressure contribution from O^+ can be as great
607 as that of H^+ [e.g., *NosÁl et al.*, 2011; *Mitani et al.*, 2019]. A rise in the density of O^+
608 in the ring current could explain our observations of enhanced plasma mass density with
609 lower magnetic field. The cold O^+ population is also thought to increase due to higher
610 outflows on the nightside during storms [e.g., *Kistler et al.*, 2016; *Gkioulidou et al.*, 2019].
611 However, it is not possible to determine from our data if these populations are responsible

612 for the plasma mass density changes, and if so, which populations dominate. Investigating
613 these changes is beyond the scope of this study.

614 From a theoretical viewpoint, the lower eigenfrequencies during storm times would
615 allow fast mode waves of given frequency to couple to field lines deeper in the magneto-
616 sphere, where they would produce standing Alfvén waves through the field line resonance
617 mechanism [e.g., *Southwood*, 1974]. Figure 7 also shows that these locations would be
618 deeper in the afternoon than the morning due to the magnetospheric asymmetry about
619 noon. Single event case studies such as *Lee et al.* [2007] and *Rae et al.* [2019] show that
620 decreased eigenfrequencies during storm times coincide with enhanced ULF wave power
621 across large regions in the inner magnetosphere. Although this study shows that lower
622 eigenfrequencies at $L > 4$ are a consistent feature of geomagnetic storms, it does not pro-
623 vide measurements of ULF wave power. The decreased eigenfrequencies are expected to
624 contribute to the increased ULF wave power due to the power law power distribution of
625 ULF waves [e.g., *Rae et al.*, 2012] but other factors may also play important roles includ-
626 ing the initial power of the fast mode waves, their frequency spectrum, their azimuthal
627 wave numbers, or changing ionospheric boundary conditions. Establishing the importance
628 of and isolating the effect of decreased eigenfrequencies on ULF wave propagation will be
629 the focus of a future study.

630 **5.2 Causes of the Variation in the Eigenfrequencies: $L < 4$**

631 By including the Tartu-Nurmijärvi pair, changes within the plasmasphere have also
632 been observed. Figure 6 shows that the eigenfrequencies and plasma mass densities had
633 a different behaviour on field lines where $L < 4$ than $L > 4$. Instead of decreasing, the
634 eigenfrequencies increase, and the plasma mass densities decrease instead of increasing.
635 The timing of this change is also delayed until the main phase, whereas changes for L
636 > 4 begin during the initial phase. Relative to quiet time, the eigenfrequencies have in-
637 creased by more than 50% partway through the recovery phase. The magnetic field change
638 is much weaker for $L < 4$ compared to $L > 4$, suggesting that the reduced plasma mass
639 density is almost entirely responsible for the increase in eigenfrequencies. It also suggests
640 that the effect of the ring current magnetic field is weaker for these inner shells. Figure 6d
641 shows a decrease in plasma mass density of more than 50%.



642 **Figure 8.** The average plasma mass density at different phases of a geomagnetic storm. Each column
 643 represents data from the 6-10, 10-14 and 14-18 MLT sectors from left to right. Each row shows the magneto-
 644 spheric state at five intervals during the average geomagnetic storm, marked on the Sym-H index plot at the
 645 bottom. Blue solid lines show the plasma mass densities at that interval of the storm, red dashed lines show
 646 the previous interval for comparison.

647 During a geomagnetic storm, the plasmopause boundary is eroded away by the in-
 648 creased convection of the Dungey cycle and a plasmaspheric plume forms [e.g., *Chappell*
 649 *et al.*, 1971; *Menk et al.*, 2014]. Regions that previously were within the plasmopause are
 650 now outside, and have a much lower plasma mass density. This would increase the eigen-
 651 frequencies [*Menk et al.*, 2004; *Dent et al.*, 2006; *Kale et al.*, 2007]. It is difficult to say
 652 where the plasmopause is in Figure 6 or Figure 7. Figure 8 shows the plasma mass den-
 653 sity data from Figure 7 as radial profiles. Each column represents one of the three MLT
 654 sectors and each row a point along the storm time axis shown at the bottom, the same as
 655 in Figures 6 and 7. The blue line shows the plasma mass density profile at that time and
 656 the dashed red line is from the time/row before to help show how the plasma mass den-
 657 sity has changed. If there is a consistent location for the plasmopause during all storms,
 658 it would be visible as a classic "knee" in this plot but because the data shows the average
 659 values of 132 storms, there is likely to be considerable variation in the plasmopause posi-
 660 tion between different storms. This has the effect of blurring out the plasmopause position
 661 and hence the "knee" is not seen in Figure 8. However, we still expect the plasmopause
 662 to retreat in this region due to enhanced magnetospheric convection. In Figures 8c and
 663 8d, for the innermost station pair, the plasma mass density decreases as expected from
 664 plasmopause erosion. The *O'Brien and Moldwin* [2003] plasmopause model shows that the
 665 plasmopause distance at noon will decrease to $L < 3$ for a -100 nT storm, which supports
 666 our observation of decreasing plasma mass density for $L \sim 4$.

667 There may still be an increase in the average ion mass due to higher densities of O^+
 668 or an increase in the mass density of the energetic population, as suggested in section 5.1.
 669 However, the observations suggest that any increase in the average ion mass is inferior to
 670 the cold plasma loss of mass from plasmopause erosion observed for $L < 4$. Hence, we
 671 see the opposite behaviour in the eigenfrequencies for the innermost L-shells.

622 **6 Conclusions**

673 This study determined how the eigenfrequency continuum changed during geomag-
 674 netic storms and how this was controlled by the underlying magnetic field strength and
 675 plasma mass density. We analysed the eigenfrequencies of magnetic field lines during 132
 676 storms using a superposed multiple-epoch analysis on cross-phase spectra derived from
 677 ground-based magnetometer stations in the range $3.15 \leq L \leq 6.42$. This region corre-
 678 sponds to a key region during geomagnetic storms because of its proximity to the ring

679 current and radiation belts. This has enabled us to determine the average time evolution of
680 the fundamental eigenfrequency during each of the three phases of a geomagnetic storm.
681 We then solved the Alfvén wave equation of *Singer et al.* [1981] using the TS05 magnetic
682 field model of *Tsyganenko and Sitnov* [2005] to determine how the plasma mass density
683 changes directly for the first time.

684 It was found that the fundamental eigenfrequency decreased in all dayside MLT sec-
685 tors during the main phase for $L > 4$ and this corresponded to a weaker magnetic field and
686 an increased plasma mass density, with a clear MLT dependence on the reduction. The
687 changes in both of these dependencies would decrease the eigenfrequency. We suggest that
688 the increase in plasma mass density is caused by an increase in Oxygen ions density.

689 For $L < 4$, the eigenfrequency increased relative to the quiet time value. This was
690 accompanied by a decrease in the plasma mass density, which is thought to be caused
691 by plasmopause erosion during the main phase of a storm. However, the magnetic field
692 strength still decreased, suggesting that the plasma mass density has a stronger influence
693 over the eigenfrequency than the magnetic field at these locations.

694 **Acknowledgments**

695 S.J.W. was supported by NERC Studentship NE/L002493/1. I.J.R. was supported
696 by STFC grants ST/S000240/1 and ST/N000722/1 and NERC grants NE/P017150/1 and
697 NE/P017185/1. J.K.S. was supported by NERC grant NE/P017185/1. M.-T. W was sup-
698 ported by NERC grant NE/P001556/1. T.K.Y. was supported by STFC grant ST/S000429/1.

699 The authors would like to thank the IMAGE magnetometer team for providing the
700 data. The data is available at: <http://space.fmi.fi/image/beta/>.

701 The OMNI solar wind and geomagnetic indices data are publicly available from the
702 NASA Space Physics Data Facility, Goddard Space Flight Center (<http://omniweb.gsfc.nasa.gov/ow.html>).

703 This research used the SPECTRE High Performance Computing Facility at the Uni-
704 versity of Leicester.

705 The list of geomagnetic storm events used in this study is available in the supple-
706 mentary information.

References

- 707
- 708 Akasofu, S.-I., S. Chapman, and D. Venkatesan (1963), The main phase of great magnetic
709 storms, *Journal of Geophysical Research (1896-1977)*, *68*(11), 3345–3350, doi:10.1029/
710 JZ068i011p03345.
- 711 Angerami, J. J., and J. O. Thomas (1964), Studies of planetary atmospheres: 1. The dis-
712 tribution of electrons and ions in the Earth's exosphere, *J Geophys Res*, *69*(21), 4537–
713 4560, doi:10.1029/JZ069i021p04537.
- 714 Berube, D., M. B. Moldwin, and J. M. Weygand (2003), An automated method for the
715 detection of field line resonance frequencies using ground magnetometer techniques, *J*
716 *Geophys Res - Space*, *108*(A9), doi:10.1029/2002JA009737, 1348.
- 717 Berube, D., M. B. Moldwin, and M. Ahn (2006), Computing magnetospheric mass density
718 from field line resonances in a realistic magnetic field geometry, *J Geophys Res - Space*,
719 *111*(A8), doi:10.1029/2005JA011450, a08206.
- 720 Bland, E. C., A. J. McDonald, F. W. Menk, and J. C. Devlin (2014), Multipoint visual-
721 ization of ULF oscillations using the Super Dual Auroral Radar Network, *Geophys Res*
722 *Lett*, *41*(18), 6314–6320, doi:10.1002/2014GL061371.
- 723 Carpenter, D. L., and R. L. Smith (1964), Whistler measurements of electron density in
724 the magnetosphere, *Rev Geophys*, *2*(3), 415–441, doi:10.1029/RG002i003p00415.
- 725 Chapman, S., and V. Ferraro (1930), A New Theory of Magnetic Storms, *Nature*, *126*,
726 129–130, doi:https://doi.org/10.1038/126129a0DO.
- 727 Chappell, C. R., K. K. Harris, and G. W. Sharp (1971), The dayside of the plasmasphere,
728 *J Geophys Res*, *76*(31), 7632–7647, doi:10.1029/JA076i031p07632.
- 729 Chi, P. J., C. T. Russell, J. C. Foster, M. B. Moldwin, M. J. Engebretson, and I. R. Mann
730 (2005), Density enhancement in plasmasphere-ionosphere plasma during the 2003 Hal-
731 loween Superstorm: Observations along the 330th magnetic meridian in North America,
732 *Geophysical Research Letters*, *32*(3), doi:10.1029/2004GL021722.
- 733 Chi, P. J., M. J. Engebretson, M. B. Moldwin, C. T. Russell, I. R. Mann, M. R. Hairston,
734 M. Reno, J. Goldstein, L. I. Winkler, J. L. Cruz-Abeyro, D.-H. Lee, K. Yumoto, R. Dal-
735 rymple, B. Chen, and J. P. Gibson (2013), Sounding of the plasmasphere by Mid-
736 continent MAGnetoseismic Chain (McMAC) magnetometers, *J Geophys Res - Space*,
737 *118*(6), 3077–3086, doi:10.1002/jgra.50274.
- 738 Chisham, G., M. Lester, S. E. Milan, M. P. Freeman, W. A. Bristow, A. Grocott, K. A.
739 McWilliams, J. M. Ruohoniemi, T. K. Yeoman, P. L. Dyson, R. A. Greenwald,

- 740 T. Kikuchi, M. Pinnock, J. P. S. Rash, N. Sato, G. J. Sofko, J.-P. Villain, and A. D. M.
741 Walker (2007), A decade of the Super Dual Auroral Radar Network (SuperDARN): sci-
742 entific achievements, new techniques and future directions, *Surv Geophys*, 28(1), 33–
743 109, doi:10.1007/s10712-007-9017-8.
- 744 Corpo, A. D., M. Vellante, B. Heilig, E. Pietropaolo, J. Reda, and J. Lichtenberger (2018),
745 Observing the cold plasma in the Earth's magnetosphere with the EMMA network, *An-
746 nals of Geophysics*, 61(0), 33, doi:10.4401/ag-7751.
- 747 Cummings, W. D., R. J. O'Sullivan, and P. J. Coleman (1969), Standing Alfvén waves in
748 the magnetosphere, *J Geophys Res*, 74(3), 778–793, doi:10.1029/JA074i003p00778.
- 749 Dent, Z. C., I. R. Mann, J. Goldstein, F. W. Menk, and L. G. Ozeke (2006), Plasmas-
750 pheric depletion, refilling, and plasmopause dynamics: A coordinated ground-based and
751 IMAGE satellite study, *J Geophys Res - Space*, 111(A3), doi:10.1029/2005JA011046.
- 752 Denton, R. E., K. Takahashi, I. A. Galkin, P. A. Nsumei, X. Huang, B. W. Reinisch, R. R.
753 Anderson, M. K. Sleeper, and W. J. Hughes (2006), Distribution of density along mag-
754 netospheric field lines, *J Geophys Res - Space*, 111(A4), doi:10.1029/2005JA011414,
755 a04213.
- 756 Du, A., W. Sun, W. Xu, and X. Gao (2005), The frequency variation of Pc5 ULF waves
757 during a magnetic storm, *Earth, Planets and Space*, 57(7), 619–625, doi:10.1186/
758 BF03351841.
- 759 Engebretson, M. J., and L. J. Cahill Jr. (1981), Pc5 pulsations observed during the june
760 1972 geomagnetic storm, *Journal of Geophysical Research: Space Physics*, 86(A7),
761 5619–5631, doi:10.1029/JA086iA07p05619.
- 762 Gkioulidou, M., S. Ohtani, A. Y. Ukhorskiy, D. G. Mitchell, K. Takahashi, H. E. Spence,
763 J. R. Wygant, C. A. Kletzing, and R. J. Barnes (2019), Low-Energy (<keV) O⁺ Ion
764 Outflow Directly Into the Inner Magnetosphere: Van Allen Probes Observations,
765 *Journal of Geophysical Research: Space Physics*, 124(1), 405–419, doi:10.1029/
766 2018JA025862.
- 767 Gonzalez, W. D., J. A. Joselyn, Y. Kamide, H. W. Kroehl, G. Rostoker, B. T. Tsurutani,
768 and V. M. Vasyliunas (1994), What is a geomagnetic storm?, *J Geophys Res - Space*,
769 99(A4), 5771–5792, doi:10.1029/93JA02867.
- 770 Greenwald, R. A., K. B. Baker, J. R. Dudeney, M. Pinnock, T. B. Jones, E. C. Thomas,
771 J. P. Villain, J. C. Cerisier, C. Senior, C. Hanuise, R. D. Hunsucker, G. Sofko,
772 J. Koehler, E. Nielsen, R. Pellinen, A. D. M. Walker, N. Sato, and H. Yamagishi (1995),

- 773 DARN/SuperDARN, *Space Science Reviews*, 71(1), 761–796, doi:10.1007/BF00751350.
- 774 Huang, C.-L., H. E. Spence, H. J. Singer, and N. A. Tsyganenko (2008), A quantitative
775 assessment of empirical magnetic field models at geosynchronous orbit during magnetic
776 storms, *J Geophys Res - Space*, 113(A4), doi:10.1029/2007JA012623.
- 777 Hughes, W. J., and D. J. Southwood (1976), The screening of micropulsation signals
778 by the atmosphere and ionosphere, *J Geophys Res*, 81(19), 3234–3240, doi:10.1029/
779 JA081i019p03234.
- 780 Hutchinson, J. A., D. M. Wright, and S. E. Milan (2011), Geomagnetic storms over the
781 last solar cycle: A superposed epoch analysis, *Journal of Geophysical Research: Space*
782 *Physics*, 116(A9), doi:10.1029/2011JA016463.
- 783 Iyemori, T. (1990), Storm-Time Magnetospheric Currents Inferred from Mid-Latitude Ge-
784 omagnetic Field Variations, *Journal of geomagnetism and geoelectricity*, 42(11), 1249–
785 1265, doi:10.5636/jgg.42.1249.
- 786 Kale, Z. C., I. R. Mann, C. L. Waters, J. Goldstein, F. W. Menk, and L. G. Ozeke (2007),
787 Ground magnetometer observation of a cross-phase reversal at a steep plasmopause, *J*
788 *Geophys Res - Space*, 112(A10), doi:10.1029/2007JA012367, a10222.
- 789 Kale, Z. C., I. R. Mann, C. L. Waters, M. Vellante, T. L. Zhang, and F. Honary (2009),
790 Plasmaspheric dynamics resulting from the Hallowe'en 2003 geomagnetic storms, *Jour-*
791 *nal of Geophysical Research: Space Physics*, 114(A8), doi:10.1029/2009JA014194.
- 792 Kistler, L. M., C. G. Mouikis, H. E. Spence, A. M. Menz, R. M. Skoug, H. O. Funsten,
793 B. A. Larsen, D. G. Mitchell, M. Gkioulidou, J. R. Wygant, and L. J. Lanzerotti (2016),
794 The source of O⁺ in the storm time ring current, *Journal of Geophysical Research:*
795 *Space Physics*, 121(6), 5333–5349, doi:10.1002/2015JA022204.
- 796 Kronberg, E. A., M. Ashour-Abdalla, I. Dandouras, D. C. Delcourt, E. E. Grigorenko,
797 L. M. Kistler, I. V. Kuzichev, J. Liao, R. Maggiolo, H. V. Malova, K. G. Orlova,
798 V. Perroomian, D. R. Shklyar, Y. Y. Shprits, D. T. Welling, and L. M. Zelenyi (2014),
799 Circulation of Heavy Ions and Their Dynamical Effects in the Magnetosphere: Re-
800 cent Observations and Models, *Space Science Reviews*, 184(1), 173–235, doi:10.1007/
801 s11214-014-0104-0.
- 802 Lee, E. A., I. R. Mann, T. M. Loto'aniu, and Z. C. Dent (2007), Global Pc5 pulsations
803 observed at unusually low L during the great magnetic storm of 24 March 1991, *Jour-*
804 *nal of Geophysical Research: Space Physics*, 112(A5), doi:10.1029/2006JA011872.

- 805 Luhr, H. (1994), The IMAGE Magnetometer Network, *STEP International Newsletter*, 4,
806 4–6.
- 807 Mardia, K. V., and P. E. Jupp (2000), *Directional Statistics*, John Wiley and Sons, Ltd.
- 808 Menk, F., Z. Kale, M. Sciffer, P. Robinson, C. Waters, R. Grew, M. Clilverd, and I. Mann
809 (2014), Remote sensing the plasmasphere, plasmopause, plumes and other features using
810 ground-based magnetometers, *J. Space Weather Space Clim.*, 4, A34, doi:10.1051/swsc/
811 2014030.
- 812 Menk, F. W., and C. L. Waters (2013), *Magnetoseismology Ground-based remote sensing
813 of the Earth's magnetosphere*, John Wiley & Sons, Inc., doi:10.1002/9783527652051.
- 814 Menk, F. W., D. Orr, M. A. Clilverd, A. J. Smith, C. L. Waters, D. K. Milling, and B. J.
815 Fraser (1999), Monitoring spatial and temporal variations in the dayside plasmasphere
816 using geomagnetic field line resonances, *J Geophys Res - Space*, 104(A9), 19,955–
817 19,969, doi:10.1029/1999JA900205.
- 818 Menk, F. W., I. R. Mann, A. J. Smith, C. L. Waters, M. A. Clilverd, and D. K. Milling
819 (2004), Monitoring the plasmopause using geomagnetic field line resonances, *J Geophys
820 Res - Space*, 109(A4), doi:10.1029/2003JA010097, a04216.
- 821 Min, K., J. Bortnik, R. E. Denton, K. Takahashi, J. Lee, and H. J. Singer (2013), Quiet
822 time equatorial mass density distribution derived from AMPTE/CCE and GOES us-
823 ing the magnetoseismology technique, *Journal of Geophysical Research: Space Physics*,
824 118(10), 6090–6105, doi:10.1002/jgra.50563.
- 825 Mitani, K., K. Seki, K. Keika, M. Gkioulidou, L. J. Lanzerotti, D. G. Mitchell, C. A.
826 Kletzing, A. Yoshikawa, and Y. Obana (2019), Statistical Study of Selective Oxygen
827 Increase in High-Energy Ring Current Ions During Magnetic Storms, *Journal of Geo-
828 physical Research: Space Physics*, 124(5), 3193–3209, doi:10.1029/2018JA026168.
- 829 Murphy, K. R., I. R. Mann, I. J. Rae, D. G. Sibeck, and C. E. J. Watt (2016), Accurately
830 characterizing the importance of wave-particle interactions in radiation belt dynamics:
831 The pitfalls of statistical wave representations, *Journal of Geophysical Research: Space
832 Physics*, 121(8), 7895–7899, doi:10.1002/2016JA022618.
- 833 Murphy, K. R., C. E. J. Watt, I. R. Mann, I. Jonathan Rae, D. G. Sibeck, A. J. Boyd, C. F.
834 Forsyth, D. L. Turner, S. G. Claudepierre, D. N. Baker, H. E. Spence, G. D. Reeves,
835 J. B. Blake, and J. Fennell (2018), The global statistical response of the outer radiation
836 belt during geomagnetic storms, *Geophysical Research Letters*, 45(9), 3783–3792, doi:
837 10.1002/2017GL076674.

- 838 NosÁf, M., K. Takahashi, R. R. Anderson, and H. J. Singer (2011), Oxygen torus in the
839 deep inner magnetosphere and its contribution to recurrent process of O+-rich ring
840 current formation, *Journal of Geophysical Research: Space Physics*, *116*(A10), doi:
841 10.1029/2011JA016651.
- 842 O'Brien, T. P., and M. B. Moldwin (2003), Empirical plasmopause models from magnetic
843 indices, *Geophys Res Lett*, *30*(4), doi:10.1029/2002GL016007, 1152.
- 844 Orr, D., and J. A. Matthew (1971), The variation of geomagnetic micropulsation periods
845 with latitude and the plasmopause, *Planet Space Sci*, *19*(8), 897 – 905, doi:https://doi.
846 org/10.1016/0032-0633(71)90141-3.
- 847 Poulter, E., W. Allan, J. Keys, and E. Nielsen (1984), Plasmatrough ion mass densities
848 determined from ULF pulsation eigenperiods, *Planet Space Sci*, *32*(9), 1069 – 1078,
849 doi:https://doi.org/10.1016/0032-0633(84)90132-6.
- 850 Rae, I. J., I. R. Mann, K. R. Murphy, L. G. Ozeke, D. K. Milling, A. A. Chan, S. R. Elk-
851 ington, and F. Honary (2012), Ground-based magnetometer determination of in situ
852 Pc4-5 ULF electric field wave spectra as a function of solar wind speed, *Journal of*
853 *Geophysical Research: Space Physics*, *117*(A4), doi:10.1029/2011JA017335.
- 854 Rae, I. J., K. R. Murphy, C. E. Watt, J. K. Sandhu, M. Georgiou, A. W. Degeling,
855 C. Forsyth, S. N. Bentley, F. A. Staples, and Q. Shi (2019), How do Ultra-Low Fre-
856 quency waves access the inner magnetosphere during geomagnetic storms?, *Geophysical*
857 *Research Letters*, *0*(ja), doi:10.1029/2019GL082395.
- 858 Rankin, R., K. Kabin, and R. Marchand (2006), Alfvénic field line resonances in arbi-
859 trary magnetic field topology, *Advances in Space Research*, *38*(8), 1720 – 1729, doi:
860 https://doi.org/10.1016/j.asr.2005.09.034, magnetospheric dynamics and the international
861 living with a star program.
- 862 Salat, A., and J. A. Tataronis (2000), Conditions for existence of orthogonal coordi-
863 nate systems oriented by magnetic field lines, *Journal of Geophysical Research: Space*
864 *Physics*, *105*(A6), 13,055–13,062, doi:10.1029/1999JA000221.
- 865 Sandhu, J. K., T. K. Yeoman, R. C. Fear, and I. Dandouras (2016), A statistical study of
866 magnetospheric ion composition along the geomagnetic field using the Cluster space-
867 craft for L values between 5.9 and 9.5, *J Geophys Res - Space*, *121*(3), 2194–2208, doi:
868 10.1002/2015JA022261, 2015JA022261.
- 869 Sandhu, J. K., T. K. Yeoman, I. J. Rae, R. C. Fear, and I. Dandouras (2017), The depen-
870 dence of magnetospheric plasma mass loading on geomagnetic activity using Cluster, *J*

- 871 *Geophys Res - Space*, 122(9), 9371–9395, doi:10.1002/2017JA024171.
- 872 Sandhu, J. K., T. K. Yeoman, and I. J. Rae (2018a), Variations of Field Line Eigen-
873 frequencies With Ring Current Intensity, *J Geophys Res - Space*, 0(0), doi:10.1029/
874 2018JA025751.
- 875 Sandhu, J. K., T. K. Yeoman, M. K. James, I. J. Rae, and R. C. Fear (2018b), Variations
876 of High-Latitude Geomagnetic Pulsation Frequencies: A Comparison of Time-of-Flight
877 Estimates and IMAGE Magnetometer Observations, *J Geophys Res - Space*, 123(1),
878 567–586, doi:10.1002/2017JA024434, 2017JA024434.
- 879 Singer, H. J., D. J. Southwood, R. J. Walker, and M. G. Kivelson (1981), Alfvén wave res-
880 onances in a realistic magnetospheric magnetic field geometry, *J Geophys Res - Space*,
881 86(A6), 4589–4596, doi:10.1029/JA086iA06p04589.
- 882 Southwood, D. (1974), Some features of field line resonances in the magnetosphere,
883 *Planet Space Sci*, 22(3), 483 – 491, doi:https://doi.org/10.1016/0032-0633(74)90078-6.
- 884 Stewart, B. (1861), On the great magnetic disturbance which extended from August 28 to
885 September 7, 1859, as recorded by photography at the Kew Observatory, *Phil. Trans. R.*
886 *Soc. Lond.*, 151, 423–430, doi:10.1098/rstl.1861.0023.
- 887 Takahashi, K., and R. E. Denton (2007), Magnetospheric seismology using multiharmonic
888 toroidal waves observed at geosynchronous orbit, *J Geophys Res - Space*, 112(A5), doi:
889 10.1029/2006JA011709, a05204.
- 890 Takahashi, K., and R. L. McPherron (1984), Standing hydromagnetic oscillations in the
891 magnetosphere, *Planet Space Sci*, 32(11), 1343 – 1359, doi:https://doi.org/10.1016/
892 0032-0633(84)90078-3.
- 893 Takahashi, K., R. E. Denton, and D. Gallagher (2002), Toroidal wave frequency at L = 6-
894 10: Active Magnetospheric Particle Tracer Explorers/CCE observations and comparison
895 with theoretical model, *J Geophys Res - Space*, 107(A2), SMP 2–1–SMP 2–14, doi:10.
896 1029/2001JA000197.
- 897 Takahashi, K., R. E. Denton, R. R. Anderson, and W. J. Hughes (2006), Mass density in-
898 ferred from toroidal wave frequencies and its comparison to electron density, *Journal of*
899 *Geophysical Research: Space Physics*, 111(A1), doi:10.1029/2005JA011286.
- 900 Takahashi, K., R. E. Denton, and H. J. Singer (2010), Solar cycle variation of geosyn-
901 chronous plasma mass density derived from the frequency of standing Alfvén waves, *J*
902 *Geophys Res - Space*, 115(A7), doi:10.1029/2009JA015243, a07207.

- 903 Takahashi, K., D. Lee, V. G. Merkin, J. G. Lyon, and M. D. Hartinger (2016), On the ori-
904 gin of the dawn-dusk asymmetry of toroidal Pc5 waves, *J Geophys Res - Space*, *121*(10),
905 9632–9650, doi:10.1002/2016JA023009.
- 906 Takasaki, S., H. Kawano, Y. Tanaka, A. Yoshikawa, M. Seto, M. Iizima, Y. Obana,
907 N. Sato, and K. Yumoto (2006), A significant mass density increase during a large mag-
908 netic storm in October 2003 obtained by ground-based ULF observations at $L \sim 1.4$,
909 *Earth Planets Space*, *58*, 617–622, doi:10.1186/BF03351959.
- 910 Tsyganenko, N. A. (1996), Effects of the Solar Wind Conditions on the Global Magneto-
911 spheric Configuration as Deduced from Data-Based Field Models, in *Proc. Third Inter-
912 national Conference on Substorms*.
- 913 Tsyganenko, N. A., and M. I. Sitnov (2005), Modeling the dynamics of the inner mag-
914 netosphere during strong geomagnetic storms, *J Geophys Res - Space*, *110*(A3), doi:
915 10.1029/2004JA010798.
- 916 Walach, M.-T., and A. Grocott (2019), SuperDARN Observations During Geomagnetic
917 Storms, Geomagnetically Active Times, and Enhanced Solar Wind Driving, *Journal of
918 Geophysical Research: Space Physics*, *124*(7), 5828–5847, doi:10.1029/2019JA026816.
- 919 Wanliss, J. A., and K. M. Showalter (2006), High-resolution global storm index: Dst ver-
920 sus SYM-H, *J Geophys Res - Space*, *111*(A2), doi:10.1029/2005JA011034, a02202.
- 921 Warner, M., and D. Orr (1979), Time of flight calculations for high latitude geomag-
922 netic pulsations, *Planet Space Sci*, *27*(5), 679 – 689, doi:https://doi.org/10.1016/
923 0032-0633(79)90165-X.
- 924 Waters, C. L., F. W. Menk, and B. J. Fraser (1991), The resonance structure of low lati-
925 tude Pc3 geomagnetic pulsations, *Geophys Res Lett*, *18*(12), 2293–2296, doi:10.1029/
926 91GL02550.
- 927 Waters, C. L., J. C. Samson, and E. F. Donovan (1996), Variation of plasmatrough density
928 derived from magnetospheric field line resonances, *J Geophys Res - Space*, *101*(A11),
929 24,737–24,745, doi:10.1029/96JA01083.
- 930 Wharton, S. J., D. M. Wright, T. K. Yeoman, M. K. James, and J. K. Sandhu (2018),
931 Cross-Phase Determination of Ultralow Frequency Wave Harmonic Frequencies and
932 Their Associated Plasma Mass Density Distributions, *Journal of Geophysical Research:
933 Space Physics*, *123*(8), 6231–6250, doi:10.1029/2018JA025487.
- 934 Wharton, S. J., D. M. Wright, T. K. Yeoman, M. K. James, and J. K. Sandhu (2019a),
935 The Variation of Resonating Magnetospheric Field Lines with Changing Geomagnetic

- 936 and Solar Wind Conditions, *Journal of Geophysical Research: Space Physics*.
- 937 Wharton, S. J., D. M. Wright, T. K. Yeoman, and A. S. Reimer (2019b), Identifying ULF
938 Wave Eigenfrequencies in SuperDARN Backscatter Using a Lomb-Scargle Cross-Phase
939 Analysis, *Journal of Geophysical Research: Space Physics*, *124*(2), 996–1012, doi:10.
940 1029/2018JA025859.
- 941 Wild, J. A., T. K. Yeoman, and C. L. Waters (2005), Revised time-of-flight calculations
942 for high-latitude geomagnetic pulsations using a realistic magnetospheric magnetic field
943 model, *J Geophys Res - Space*, *110*(A11), doi:10.1029/2004JA010964.
- 944 Yue, C., J. Bortnik, W. Li, Q. Ma, C.-P. Wang, R. M. Thorne, L. Lyons, G. D. Reeves,
945 H. E. Spence, A. J. Gerrard, M. Gkioulidou, and D. G. Mitchell (2019), Oxygen Ion
946 Dynamics in the Earth's Ring Current: Van Allen Probes Observations, *Journal of Geo-*
947 *physical Research: Space Physics*, *0*(ja), doi:10.1029/2019JA026801.

Figure 1.

Initial

Main

Recovery

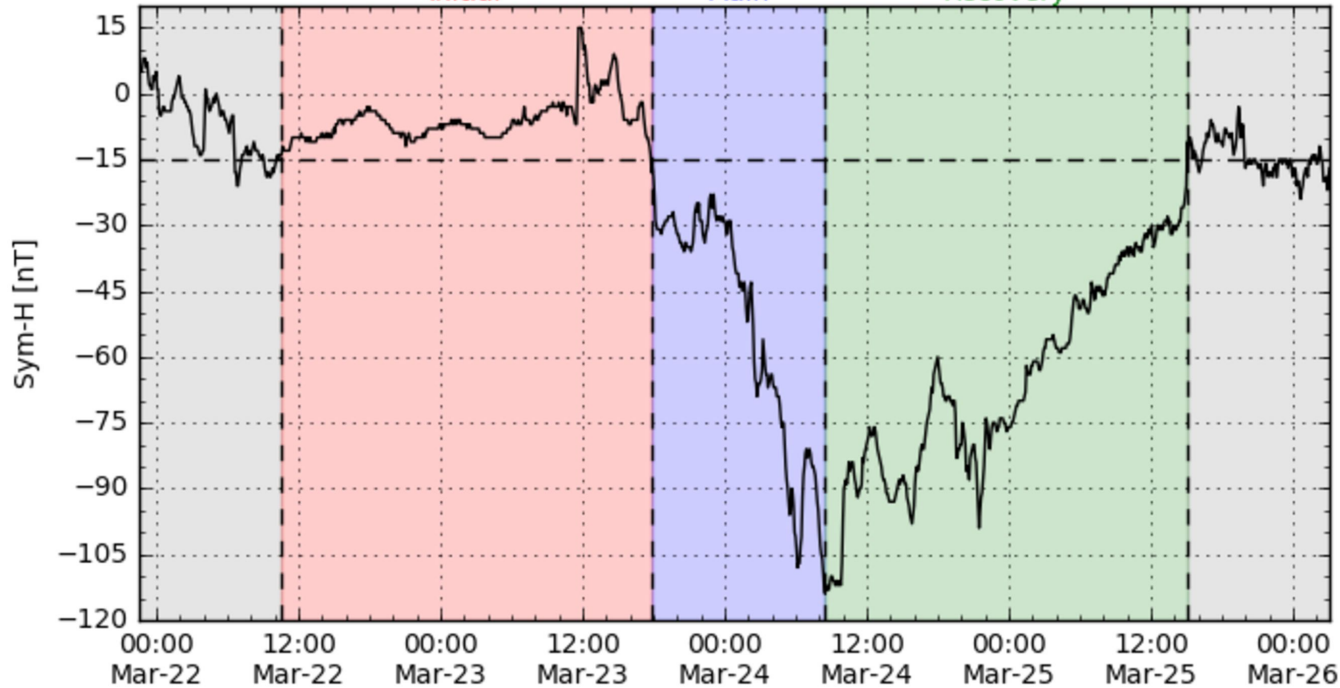


Figure 2.

Storm time cross-phase

22 Mar 2002 - 25 Mar 2002

Pello - Muonio

Storm 1: 0-24 MLT

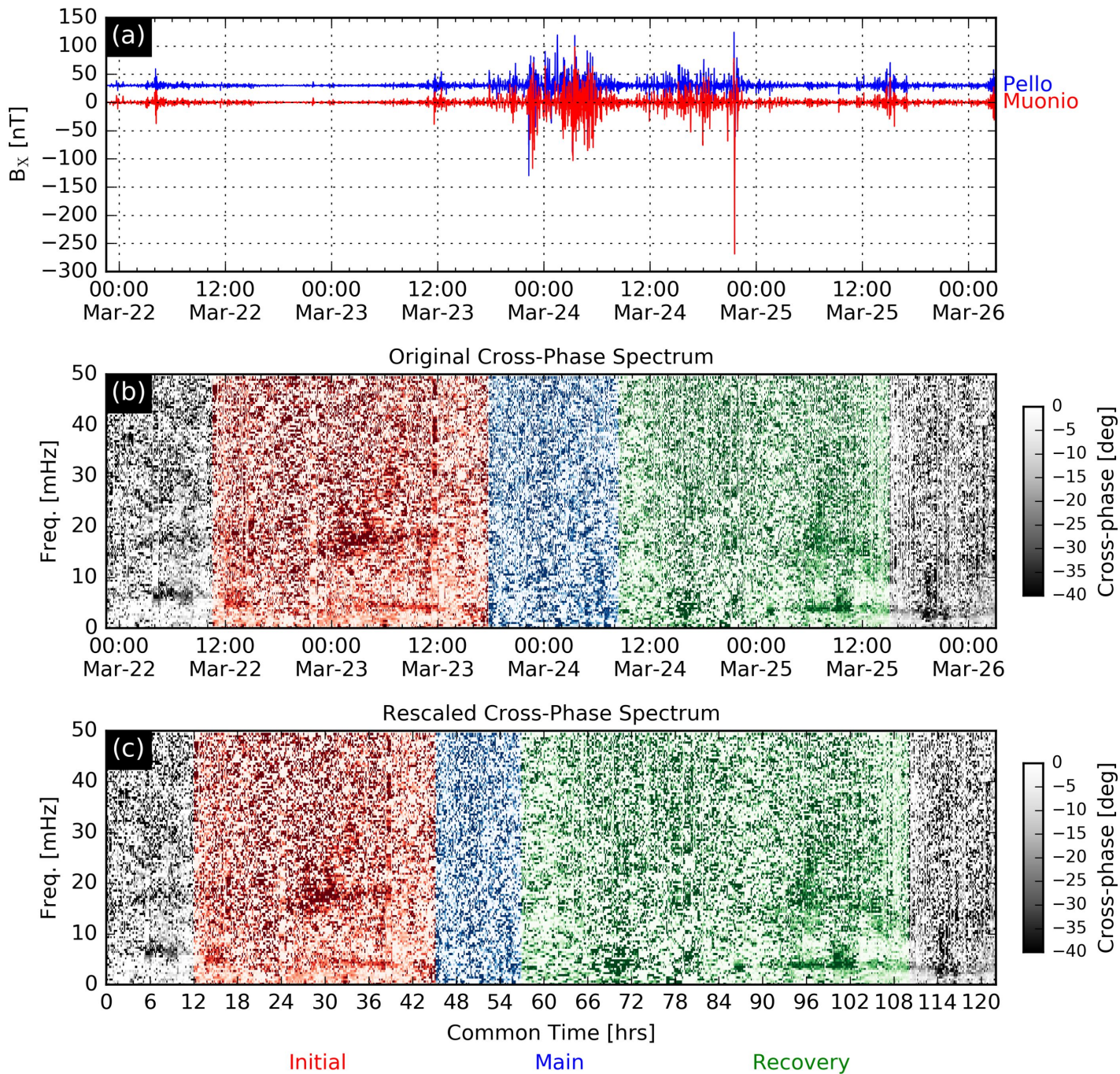


Figure 3.

Average storm time cross-phase: 10-14 MLT

132 storms
PEL - MUO: L = 5.21

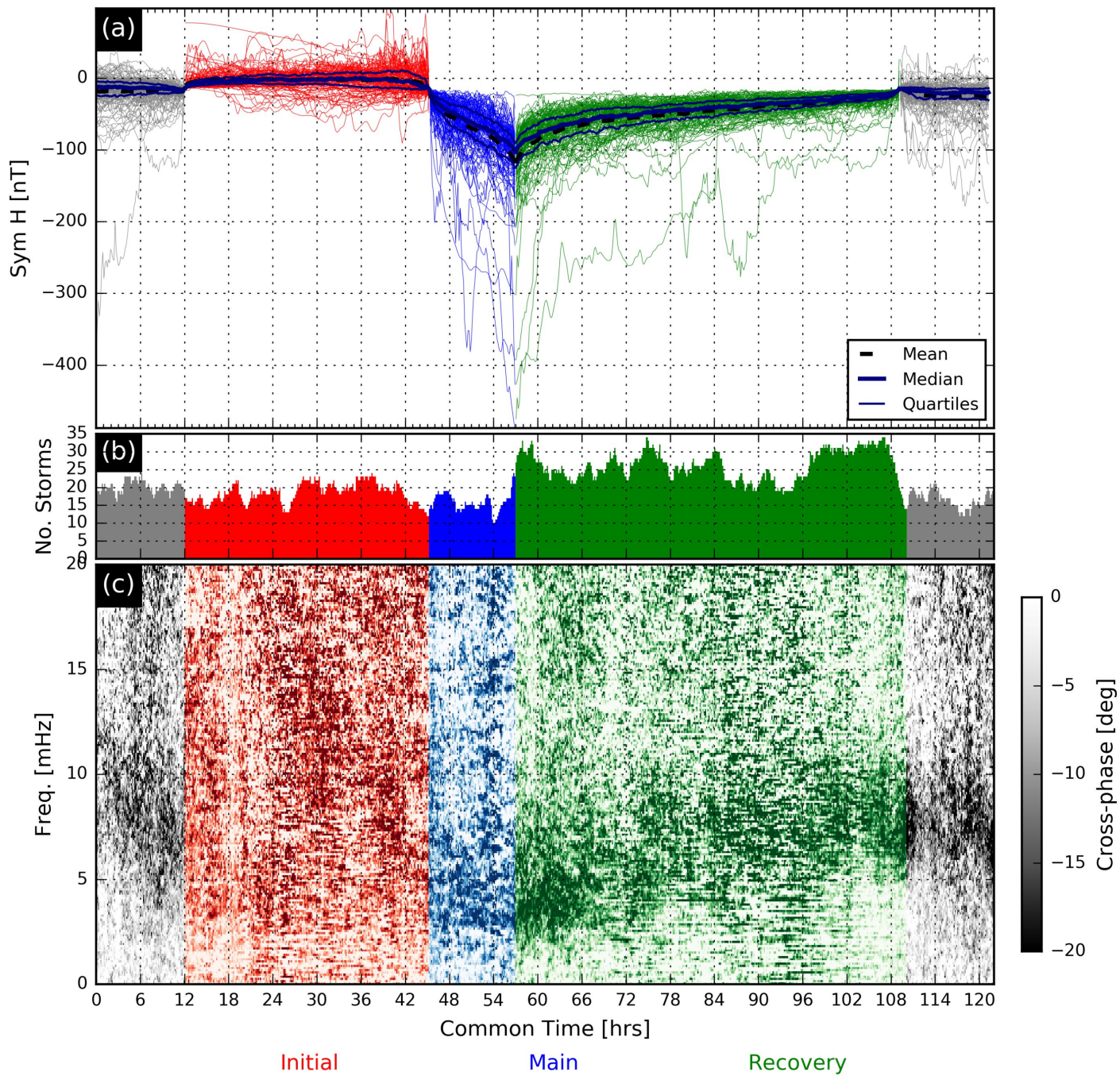


Figure 4.

Average storm time cross-phase: 10-14 MLT

132 storms
Pello - Muonio

Averaging Box: 4.0 mHz - 4.0 hrs

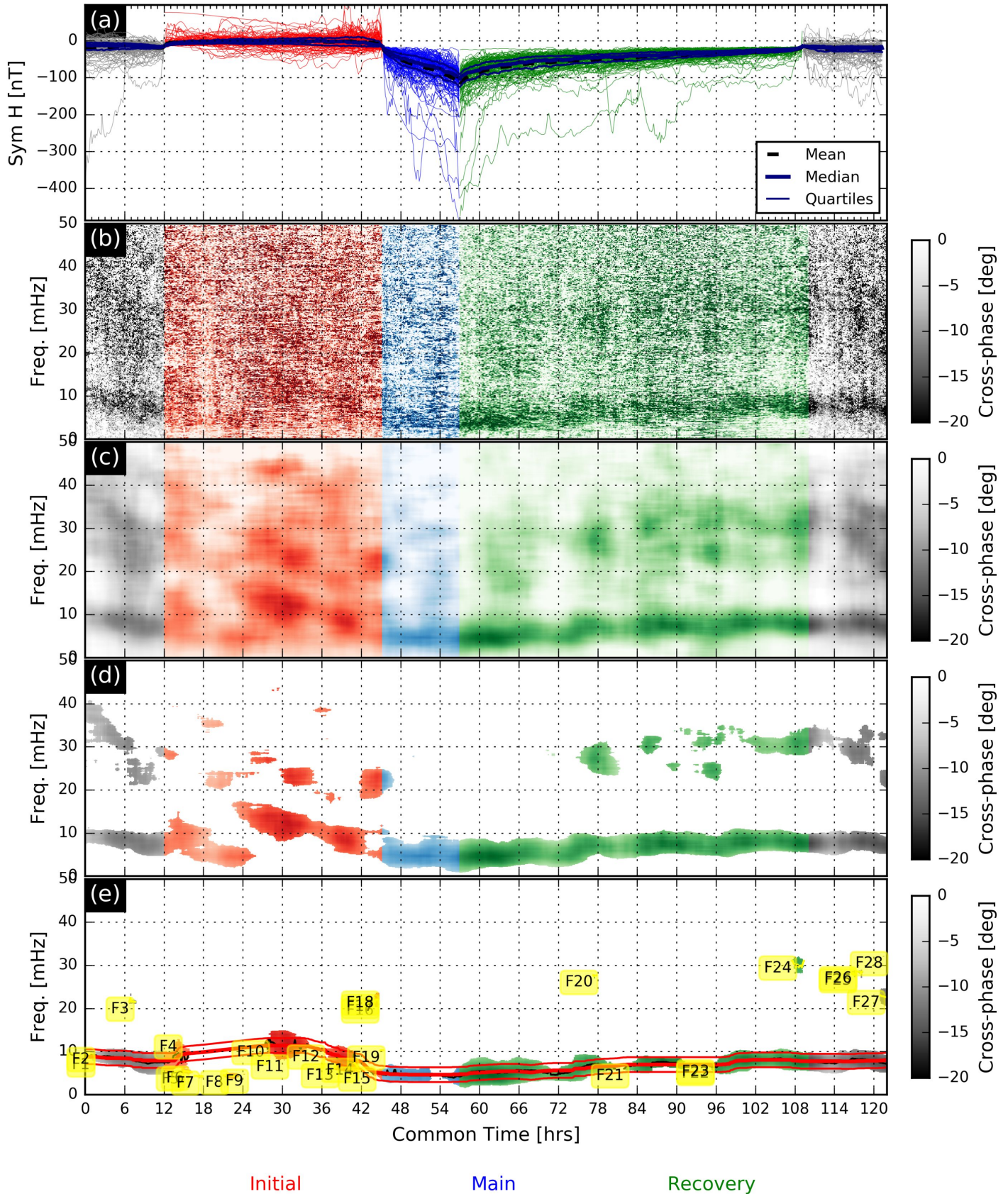


Figure 5.

Average storm time cross-phase: 10-14 MLT

132 storms
 Pello - Muonio
 L = 5.21

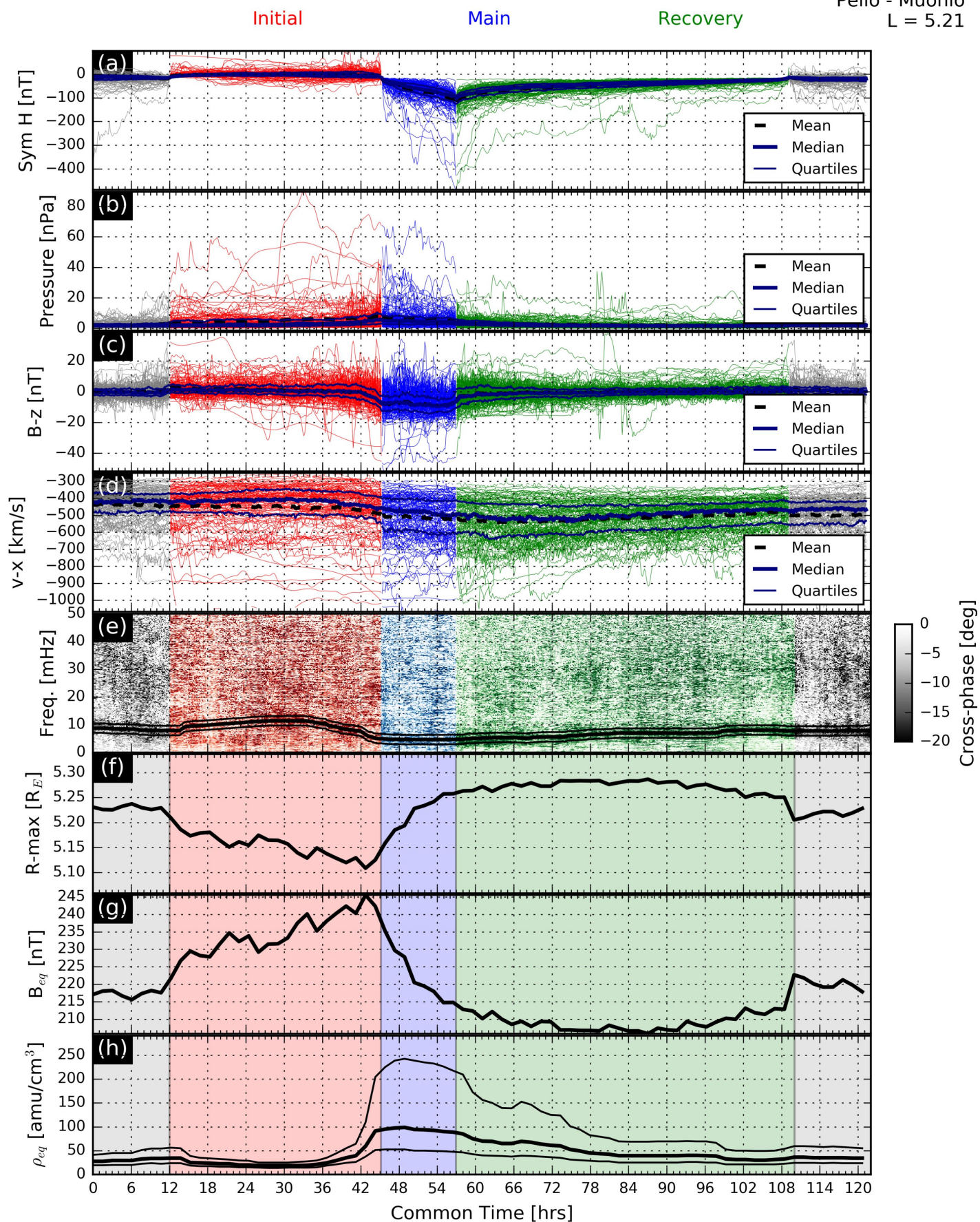


Figure 6.

Eigenfrequencies

Magnetic Field

Plasma mass densities

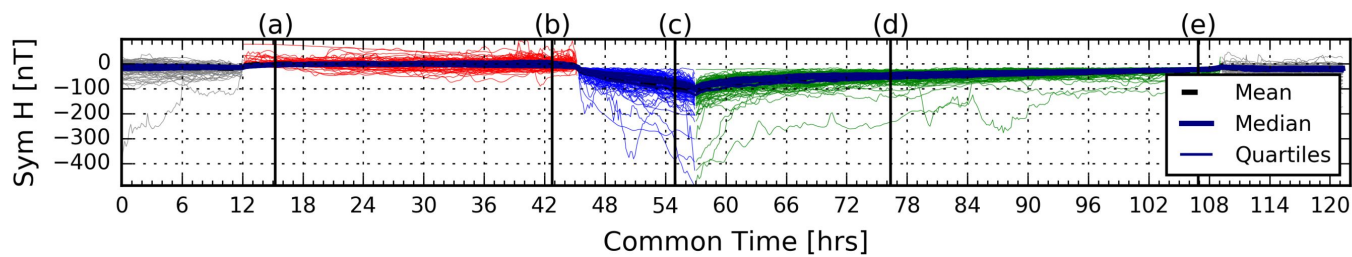
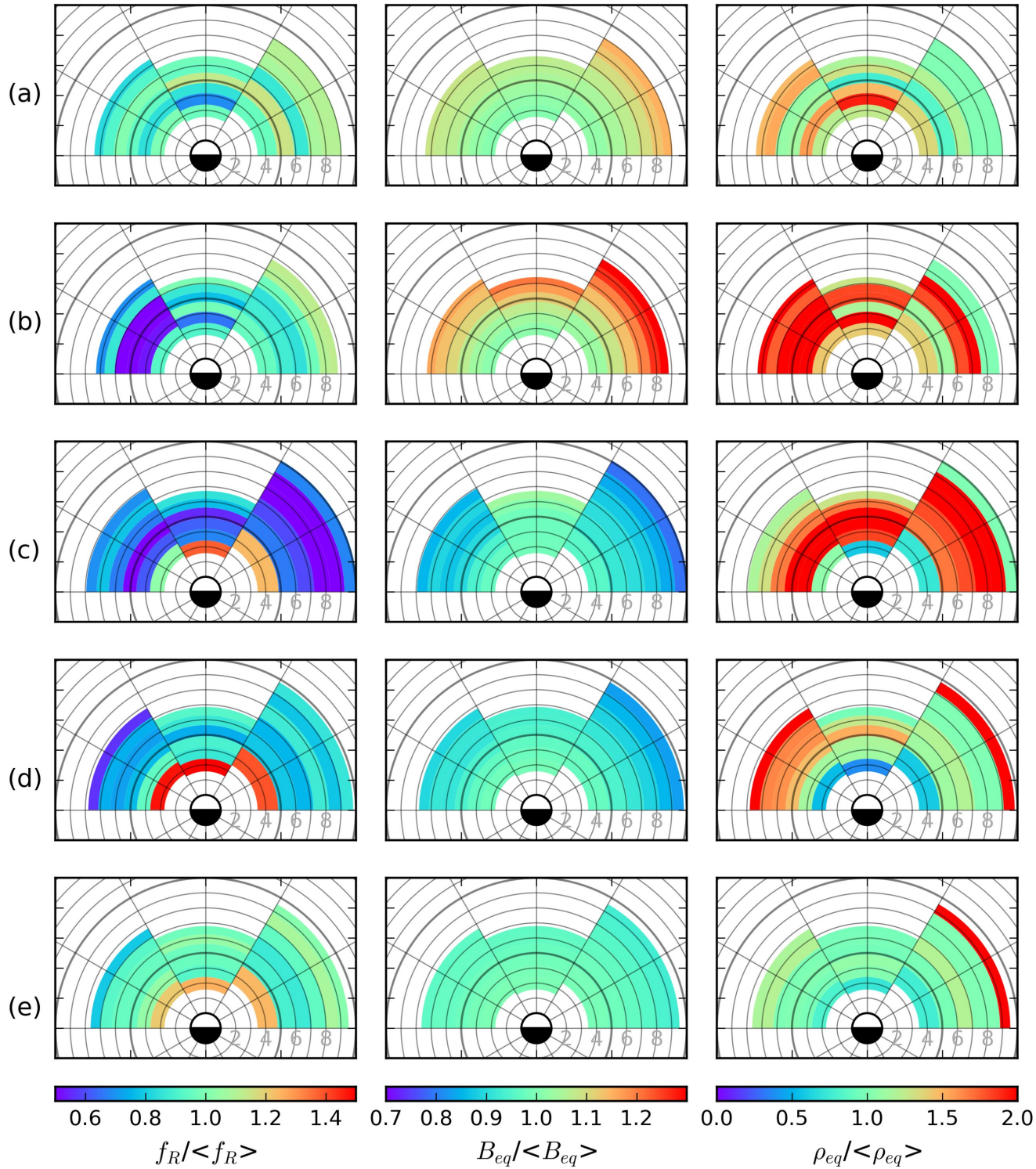


Figure 7.

Figure 8.

Radial Plasma Profiles

